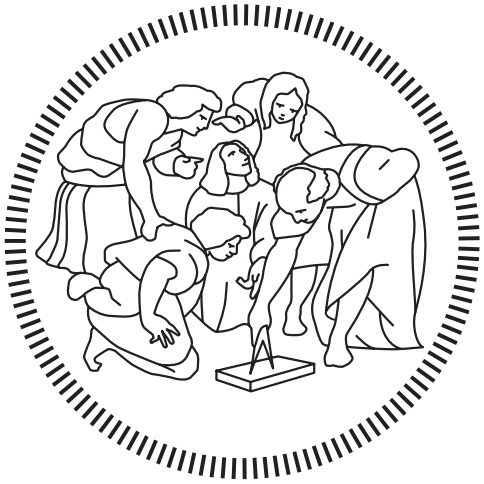

POLITECNICO DI MILANO

School of Industrial and Information Engineering
Department of Aerospace Science and Technology
MSC in Aeronautical Engineering

THE INFLUENCE OF ENDPLATE GEOMETRY AND TIP STRUCTURE ON WHEEL WAKE AERODYNAMICS

Author:
Marco Leali
928015

Supervisor:
Prof. Maurizio Quadrio
Co-Advisors:
Dr. João Patrício Soares Correia
Prof. André Resende Rodrigues da Silva

Academic Year 2020 – 2021

Abstract

The present study focuses on investigating the aerodynamic interaction between the endplate, blended to a three-element front wing, and a wheel in ground effect regarding the Formula 1 regulations change set for 2022. The simplification of the aerodynamic design, by reducing the several components on the car, is one of the main changes. The project purpose was accomplished by conducting a three-dimensional computational analysis; a steady RANS simulation approach was adopted on a simplified one-quarter CAD model, built from the ground up following the regulations imposed by the FIA.

The aim of this thesis was to investigate how changing the front wing pressure distribution affected wheel aerodynamics, which due to its proximity to the chassis will, in turn, influence the underbody's feeding process. This was completed by varying the endplate geometry, testing several layouts: canard height, canard angle of attack, endplate side shape and footplate addition. The CFD study aimed at analysing and comprehending the flow over the wing and then over the wheel by determining the flow mechanism and energy losses. For the footplate case, in addition, a force analysis over the front wing has been carried since it showed a significant efficiency variation than the other sets.

The flow investigation demonstrated that the wheel wake structure is considerably influenced by the endplate configuration displaying different behaviour for each set considered. This is related to changes in positions and strength of the vortices shedding from the endplate and flowing around the wheel. These variations then directly disturb the wheel wake, exhibiting different swirling structures which evolve in disparate ways and affect the underbody's efficiency.

Keywords: *Aerodynamics, CFD, RANS, Formula 1, Wheel, Endplate, Wing, Ground Effect, Vortex*

Sommario

Il seguente studio ha l'obiettivo di analizzare l'interazione aerodinamica in effetto suolo tra un'endplate, congiunta ad un'ala frontale di tre elementi, e uno pneumatico di una vettura di Formula 1, rispettando il nuovo regolamento che sarà introdotto dalla stagione 2022. Una delle principali e più drastiche novità riguarderà l'aerodinamica, la quale diventerà molto più semplice a seguito della minor complessità dei vari componenti. L'obiettivo di questa tesi è stato raggiunto conducendo un'analisi numerica tridimensionale; il modello utilizzato per lo studio è un CAD semplificato, disegnato seguendo le limitazioni imposte dalla FIA. La fase di simulazione numerica, è stata svolta impiegando delle RANS stazionarie.

Lo scopo di questo progetto è di osservare come una variazione del campo di pressione nei pressi dell'ala frontale influenzi l'aerodinamica dello pneumatico e, vista la vicinanza di quest'ultimo con il telaio, il processo di alimentazione del sottoscocca. Per condurre questo tipo di analisi, sono state analizzate molteplici geometrie dell'endplate: l'altezza del canard, l'angolo di attacco dello stesso, il profilo laterale dell'endplate e l'aggiunta di una footplate. L'indagine ha come scopo quello di comprendere e analizzare il flusso attorno a questi componenti determinando i meccanismi principali e le perdite di energia. Inoltre per quanto riguarda il caso con la footplate, è stata condotta un'analisi delle forze sull'alettone frontale, in quanto questa configurazione ha manifestato un'importante variazione delle forze agenti sull'ala rispetto agli altri casi.

La ricerca ha dimostrato che la scia prodotta dallo pneumatico è influenzata in maniera significativa dalla struttura dell'endplate, mostrando diversi comportamenti a seconda della geometria analizzata. Queste differenze sono associate alle diverse posizioni e intensità dei vortici che diffondono dall'ala e interagiscono con la ruota, influenzando direttamente la scia dello pneumatico e l'efficienza del sottoscocca.

Parole chiave: *Aerodinamica, CFD, RANS, Formula 1, Pneumatico, Endplate, Ala, Effetto Suolo, Vortice*

Acknowledgements

First of all, I would like to thank my co-advisor Professor André Silva, despite the difficult period everybody is going through, he welcomed me and met my desire to develop a thesis during my Erasmus period in Portugal. Without him, this amazing experience would not have been possible. Obrigado.

Secondly, I must thank my other co-advisor João Correia for showing me the right path with its tips and suggestions about this complicated but equally fascinating topic, that is motorsport aerodynamics. With the insights regarding this world, I had the opportunity to appreciate the various facets of his profession. Obrigado.

Thanks also to Professor Maurizio Quadrio, who supported my choice and gave his willingness to be my supervisor even though this was not one of his projects.

Un grazie va sopratutto ai miei genitori, nonostante i problemi degli ultimi anni, non avete mai smesso di sostenermi ed in particolare, senza di voi non sarebbe stato possibile iniziare questo percorso di studi che mi ha permesso di crescere e diventare un uomo grazie alle varie esperienze lontano da casa. A mio fratello Andrea, per le prelibatezze in veste di fornaio e pasticcere che hanno accompagnato i miei rientri. A Luna, la migliore compagna di studi che potessi avere.

A Greta per avermi sopportato più che supportato in questi ultimi anni. Per i vari momenti di svago e di leggerezza che mi hai dato, senza di te sarebbe stato tutto più difficile.

A Pietro, Delo, Gio e Fede, gli amici di una vita, dei fratelli, per esserci sempre stati nonostante il mio poco tempo a casa. Al Gaiz, per gli splendidi quattro anni insieme a Milano, grazie per i tuoi fantastici outfit da biblioteca e i buchi nei muri. Agli amici dell'Erasmus, in particolare Malpa e Pacho, grazie davvero per aver condiviso la migliore esperienza della mia vita; sono partito con una pandemia e mi sono ritrovato con dei fratelli. Agli amici di "Pavia all'8/La Rosa News 24", per aver rallegrato le giornate uggiose e altrettanto roventi al Poli. In particolare a Jack e Mane, per l'aiuto e la compagnia in questi ultimi due anni.

A tutti i miei parenti, nonni e zii, per gli insegnamenti di una vita e il vostro appoggio sempre.

Last but not least, thanks to the inspiration of a lifetime, Kobe Bean Bryant, with your example this little insecure child has learnt to believe in himself.

Contents

List of Figures

List of Tables

List of Symbols

Uppercase

C_D	—	Drag coefficient.
C_L	—	Lift coefficient.
C_p	—	Pressure coefficient.
C_pT	—	Total pressure coefficient.
D	—	Wheel diameter (mm).
L	—	Car Length (mm).
M	—	Mach number.
P	—	Mean pressure (Pa).
Re	—	Reynolds number.
$\mathbf{S}$	—	Symmetric component of velocity gradient.
U_i	—	Mean velocity (m/s).
U_∞	—	Inlet velocity (m/s).

Lowercase

c	—	Airfoil chord (mm).
p	—	Pressure field (Pa).
$p^{'}$	—	Pressure fluctuations (Pa).
p_t	—	Total pressure (Pa).
u_i	—	Velocity field (m/s).
$u_i^{'}$	—	Velocity fluctuations (m/s).
x_i	—	Cartesian coordinates (m).
y^+	—	Non-dimensional normal wall distance.

Greek letters

ε	—	Turbulence dissipation (J/(kg $\cdot$ s)).
k	—	Turbulent kinetic energy (J/kg).
λ	—	Eigenvalues.
ν	—	Kinematic viscosity (m^2/s).
ω	—	Specific turbulence dissipation (1/s).
ω_z	—	Vorticity in z-direction (1/s).
$\mathbf{\Omega}$	—	Antisymmetric component of velocity gradient.

ρ — Density (kg/m^3).

Math operators

∇ — Nabla.

Acronyms

CAD — Computer-Aided Design.
CFD — Computational Fluid Dynamics.
CPU — Central processing unit.
DES — Detached Eddy Simulation.
DNS — Direct Numerical Simulation.
FIA — Fédération Internationale de l'Automobile.
FMG — Full Multigrid.
LBM — Lattice Boltzmann method.
LDA — Laser Doppler Anemometry.
LES — Large Eddy Simulation.
PIV — Particle Image Velocimetry.
RAM — Random Access Memory.
RANS — Reynolds-Averaged Navier-Stokes.
R&D — Research and Development.
RS — Reference Surfaces.
RV — Reference Volumes.
SIMPLE — Semi-Implicit Method for Pressure-Linked Equations.
SST — Shear-Stress Transport.
TUI — Text User Interface.

Chapter 1

Introduction

1.1 Context

The study of aerodynamics is usually associated with aircraft design as it is part of the developing process. However, road vehicles, especially racing cars, make use of the airflow around them to optimise cooling and performance. The first involves engine and brakes because it is important to keep their temperature to a level where they operate at high efficiency. The second one is about two main objectives: reducing drag and increasing downforce.

Aerodynamic performance has been considered in the design of Formula 1 cars since the beginning of the competitions in the early 1950s. However, its role was secondary and aerodynamic considerations were focused especially on reducing the amount of drag generated in the car. The first appearance of wings in Formula 1 cars took place in 1968 when Colin Chapman introduced front and rear wings on the *Lotus 49* (Fig. 1.1) to achieve aerodynamic downforce [1]; this innovation highlighted the importance of aerodynamic design on racing cars to increase their performances [2].

Downforce can increase the tyre maximum lateral and longitudinal forces, resulting in an increment in car cornering speed and an improvement in car acceleration and braking performance. Additionally, the most important influence of the drag reduction is the increment in car maximum speed. Improving one of these two parameters will always affect the other, therefore a compromise is required.

Another aspect of race cars that must be optimised is the total aerodynamic balance between the front and rear axle downforce; this is a fundamental aspect in order to reach the best performance on track. Although the aerodynamics of these inverted wings improved, there was no large advance in performance until 1977 when the full ground effect was incorporated. The car underbody was shaped in such a way to exploit the Venturi's effect and generate downforce. Side skirts sealed the air under the car improving this effect. This technique improved over the years increasing cars' cornering speed. However in 1989, it was banned by the FIA because it was considered too dangerous. A flat bottom was then introduced, shifting the R&D of aerodynamics to other components on the car.

Figure 1.1: First appearance of front and rear wing on the Lotus 49 in 1968 [1].

Today, aerodynamics is one of the most important areas in the design of a Formula 1 car. Almost all generated downforce is provided by three main aerodynamic devices: front wing, rear wing and diffuser-floor. As explained before, they cannot be designed separately because an optimal balance should be found to guarantee excellent force balance on the tyres. The pressure centre, when placed too rearward leads to front wheels with less maximum force and the car understeers. If it is placed in front of the car, the rear wheels will have less maximum lateral force and hence the car oversteers.

The front wing of a Formula 1 car is the frontmost component and has changed a lot along the years. It has a negative angle of attack and additional devices can be found, such as flaps, Gurney[1] flap or endplates. Moreover, its design influences the aerodynamics of all the car, affecting the tyres, the flow of the underbody diffuser and the rear wing. The flow around the tyres is very complex, this is why it is important a good design of the front wing. The aim is to reduce as much as possible the drag the wheels generate, which accounts for about 40% of the overall car drag, by directing the flow around them and increasing the performance.

Since the 2010s, the FIA regulations have been very strictly and did not allow for new innovative concepts, but the wind tunnel testing and the introduction of Computational Fluid Dynamics (CFD) methods have allowed teams to develop high performances multi-elements front wings. However, wind tunnel testing and all the flow visualisation technique such as PIV (Particle Image Velocimetry), oil flow and LDA (Laser Doppler Anemometry) are costly. As computational power has increased in the last decade, CFD has become a valid alternative to wind tunnel testing allowing the study of flow in ways not possible experimentally. Although its use is still limited by resources and accuracy.

For the year 2022, a new set of regulations [3] have been developed, introducing a totally different aerodynamic concept in Formula 1 cars, leading to the start of a new

[1] *The Gurney flap is a small tab projecting from the trailing edge of a wing. It serves essentially the same purpose as the complex flaps on an aircraft wing. It increases lift on aircraft or, in racing car case, downforce.*

era. In 2022 cars will have a completely new design philosophy and a striking new look: sweeping bodywork, simplified front wing, bigger rear wings, increased underbody aerodynamics, wheel wake control devices, simplified suspension and low-profile tyres with 18-inch rims. All these new rules aim to improve the spectacle, focusing on the aerodynamic performance of the cars located in the wake of the previous cars, boosting overtake possibilities.

1.2 2022 Formula 1 Technical Regulations

The 2022 World Championship is due to see an overhaul of the technical regulations. These changes had been planned for introduction in 2021, with teams developing their cars throughout 2020. However, the debut of the regulations was delayed until the 2022 championship in response to the COVID-19 pandemic.

Mainly all the new regulations have been developed in order to increase the spectacle. The new design of the aerodynamic devices are aimed at boosting overtake possibilities and challenges between drivers. An overview of some of the new rules is listed below:

- Reintroduction of the ground effect since it was banned in the 80s. Therefore the bodywork will be simplified (Fig.1.2) making the underbody the main source of downforce. This aims to reduce the turbulent air provoked by the very complex design of the current wings allowing the following cars not to lose 40% of downforce, which are the actual losses, and limiting them to 5-10%.
- The front wing will be also directly connected to the nosecone allowing the teams to exploit only the wing area. The front wing will be simplified reducing the number and complexity of aerodynamic elements.
- The rear wing will be wider and mounted higher than in previous years, with additional restrictions in place to limit the teams' ability to use the car's exhaust gases to generate downforce.
- Teams will be further restricted in the number of aerodynamic car upgrades over race weekends, and the number of in-season aero upgrades.
- Introduction of certain standardised parts (such as fuel pumps), parts that must have a prescribed design (such as wheel covers), and increased restrictions on the number of times some components can be replaced.
- Tyre will move from 13-inch to a low-profile 18-inch wheels.
- The number of wind tunnel runs teams can do each week has been reduced, with emphasis put on using CFD (Computational Fluid Dynamics) simulations over physical ones.
- For the first time, Formula 1 will introduce spending restrictions to make the sport fairer and more sustainable. A cost cap will be set at $\$175M$ per team, per year, and applies to anything that covers on-track performance – excluding marketing costs, the salaries of drivers and of the top three personnel at any team.

Figure 1.2: Formula 1 2022 prototype. The bodywork is cleaner and simpler. Despite the current cars, not so many aerodynamic devices are present as suggested by FIA new regulations, simplifying the body and the flow around the car.

1.3 Objectives

The main goal of this thesis is to analyse the influence that the endplate and tip structure of the front wing of a Formula 1 car have on the behaviour of the tyre wake aerodynamics. This study takes into consideration the new regulations [3] introduced by the FIA for the 2022 championship for the design of the CAD geometry. The introduction of these new regulations, restrict the design of aerodynamic devices, aiming simplify the geometry in order to decrease the differences among the teams. These changes reduce the capability of teams controlling the front wheel wake. Therefore, this work is a first approach at finding what changes they can explore to regain some control.

As already explained, the interaction between the front wing, the endplate in particular for this project, and the wheel will be the main objective. Therefore the design will focus on the front right half of the car, not considering components unnecessary for this analysis. Different geometries of the endplate will be compared and analysed, by looking at some parameters such as force coefficients, total pressure coefficient and streamwise and vertical velocities.

In this study, relying on the new rules, the focus will be on the wheel wake behaviour in order to investigate how energy losses affect the wake and the underbody's feeding process. Indeed the reintroduction of ground effect, relying less on the overbody aerodynamic components, requires more energetic flow underneath the car. The various geometries will be tested through a CFD analysis developed with the commercial software Ansys Fluent 2019 R3 [4].

1.4 Outline of the thesis

The thesis framework consists of the following chapters:

2. **Literature Review**: in this chapter, an overview of the most interesting and accepted studies about the aerodynamics of the various components of a Formula 1 car is done. The chapter will focus firstly on the isolated wing in ground effect, the wheel and the endplate, to conclude with a review of the combined case.

3. **Numerical Setup**: here, the focus will shift to the CAD model development, followed by the mesh generation and computational domain definition. Following, an overall description of the numerical approach adopted is given by looking at the governing equations, turbulence model, boundary conditions and solver setup adopted. Last but not least, a validation of the numerical model is done.

4. **Results**: in this chapter, firstly it is exposed the grid independence study. In the second part, a discussion and analysis of the flow around the wing and wheel for the four cases is done comparing the various geometries adopted to a reference model.

5. **Conclusions and future development**: in this last chapter, some last considerations are proposed, together with some remarks for a future development.

Chapter 2

Literature Review

The front wing of a Formula 1 car affects the aerodynamics of the elements downstream, such as tyres, rear wing and diffuser. Small changes can have large effects on the total balance. Therefore, it is important to understand the physics and what happens to the flow around all the devices involved.

Due to the very specific application and the competitive nature of the motorsport industry, most of the studies carried along the years have been kept confidential, therefore very little material has been published. The aerodynamics relative to this subject has been broken down to smaller sections in which the literature is more available: vortex behaviour and structure, front wing operating in ground effect and wheel aerodynamics; thus an overview of these topics follows.

2.1 Vortex Behaviour

Aerodynamic design of race cars is very much orientated towards using turbulence, therefore the flow control through vortices is fundamental in order to generate or enhance the downforce and minimise the drag. In the majority of applications, vortices are influenced by the interaction with multiple bodies that is the case of a Formula 1 car. Hence their behaviour can be very different to the one expected for an isolated vortex. In an open wheel race car, vortex cores interact one each other. Not only, the influence of the ground such as the presence of the wheel, which can lead a vortex to the breakdown phenomenon, should be considered. Therefore many general characteristics can be discussed starting from the identification and visualisation of vortices to the merging and breakdown mechanisms.

The vortices more relevant for the current problem, result from flow separation at sharp edges of the geometry due to a pressure difference between both sides of the component. Two types of vortices can be identified in this case: longitudinal vortices originate from edges that are more or less aligned with the flow and transverse vortices, resulting from edges perpendicular to the flow, such as blunt trailing edges and Gurney.

The endplate vortices are of the first type and play an important role as downforce enhancing and limiting mechanism for wings in ground effect. The pressure difference, which causes endplate and wing tip vortices, induces a circulation around the edge. Here

the combination of the pressure difference and the opposing flow direction causes the flow to swirl and detach from the wing, thus forming a vortex with its axis aligned with the flow in streamwise direction.

Therefore vortices can be described as having a swirling motion around an axis. The vortex core along the axis can be distinguished from the outer rotating flow. In general, vortex cores are characterized by having low pressure. Within the vortex, the centrifugal force generates a strong radial pressure gradient, with the minimum pressure occurring along the vortex axis. The tangential velocity in the core centre is zero and reaches a maximum at the edge of the core after which then it reduces to the outer flow value.

No single definition of vortex is universally accepted nowadays as Chakraborty explains [5]. Many definitions have been proposed in the past years, most of them refer to a vortex such as: pressure minimum core, closed or spiralling streamlines or a threshold vorticity level. Therefore a practical problem in studying vortices is the identification and visualisation of the swirling structures. Anyway, there are two properties that everyone agrees on in order to define a vortex [6]:

- The vortex core must have a vorticity and therefore a non-zero circulation.
- Vortex structure characteristics must be galilean invariant.

The most common identification methods are based on the local analysis of the velocity gradient tensor $\nabla \boldsymbol{u}$, that is why these are recognised as local methods. However, these methods, being based on local information of the flowfield, are not able to get the connections that may exist between fluid elements with distance equivalent to the vortex size. A non-local approach has been developed by Cucitore et al. [7]. This method is galilean invariant and uses the intuitive notion that the change in the relative distance between particles inside a vortex structure is small. Anyway, this method even behaving in a good way is computationally expensive compared to a local approach. Therefore, it is more suitable to exploit a local method if the computational power at disposal is not considerable.

Jeong and Hussain [6] reviewed several local identification methods, each one with their own limitations. They came out by defining a new method (λ_2-criterion) and redefining the Q-criterion. These new definitions discard two effects that show the inconsistency between the existence of a pressure minimum and the existence of a vortex core:

- Unsteady straining, which can create a pressure minimum without involving a vortical or swirling motion.
- Viscous effects, which can eliminate the pressure minimum in a flow with vortical motion.

The quantity Q is then defined as follows:

$$Q = -\frac{1}{2} tr(\mathbf{S}^2 + \mathbf{\Omega}^2) \tag{2.1}$$

where $\mathbf{S}$ and $\mathbf{\Omega}$ are respectively the symmetric and antisymmetric components of the velocity gradient tensor $\nabla \boldsymbol{u}$. The two components of the tensor are defined in the following way:

$$S_{ij} = \frac{1}{2}(u_{i,j} + u_{j,i}) \tag{2.2}$$

$$\Omega_{ij} = \frac{1}{2}(u_{i,j} - u_{j,i}) \tag{2.3}$$

By discarding the two effects listed above, the authors observed that the pressure minimum is dependent on the eigenvalues of the tensor $\mathbf{S}^2 + \mathbf{\Omega}^2$, which by definition is symmetric and with real eigenvalues. Assuming to sort them in the following manner, $\lambda_1 \geqslant \lambda_2 \geqslant \lambda_3$, the criterion request reduces to $\lambda_2 \leqslant 0$.

In a plane, in a two-dimensional flow field, the Q-criterion is equivalent to the λ_2-criterion and a vortex core is subsequently defined as a connected region with two negative eigenvalues of $\mathbf{S}^2 + \mathbf{\Omega}^2$. Indeed the eigenvalues of $\mathbf{S}^2 + \mathbf{\Omega}^2$ and Q for a general case, are related by the following expression:

$$Q = -\frac{1}{2}tr(\mathbf{S}^2 + \mathbf{\Omega}^2) = -\frac{1}{2}(\lambda_1 + \lambda_2 + \lambda_3) \tag{2.4}$$

The Q-criterion, or λ_2-criterion, can not only be used as a vortex core identification method, but also to visualise vortices. Exploiting the Q-criterion method, isosurfaces can be generated, giving an overview of the vortical structures, however the choice of the visualisation threshold is still arbitrary. This is important to be kept in mind when analysing isosurfaces of Q, because a lower value could show vortex merging while this phenomenon can not be distinguished for higher value of Q. In this work, this method is exploited to visualise the swirling structures around the endplate to give a qualitative representation and not as an identification technique. The vortices are identified referring to previous studies and in an intuitive way based on the aerodynamic knowledge that a pressure difference favours the air to roll from a higher pressure zone to a lower one. Another important aspect to highlight is the difference in the velocity employed. In this study a RANS approach is used, hence the Q-criterion will make use of the mean velocity; visualising mean data will give the flowfield an average overall behaviour, losing especially small scale structures.

There are various stages in the "life" of a vortex that generally involve formation, roll up, the development, the merging (if two or more vortices are close to each other) and the breakdown. When multiple vortices are located close together in a flow field, they may interact. This mechanism may consist in a change of position of the vortices because influenced one another by their own velocity. If vortices of like sign come sufficiently close, the viscous phenomenon of merging can take place. Counter-rotating vortex merging may also take place in many applications. Regarding our field of study, the vortices that are shedding from the front wing and endplate will have the same sense of rotation.

A good analysis was carried by Cerretelli and Williamson [8]. In their paper they split the mechanism of vortex merging into four stages: diffusive stage, convective merging phase, a briefly second diffusive stage and a final diffusion of the merged elliptic vortex.

In the first stage, the two vortices begin to rotate about one another due to the velocity they induce, maintaining the core distance. As the phase name suggests, the

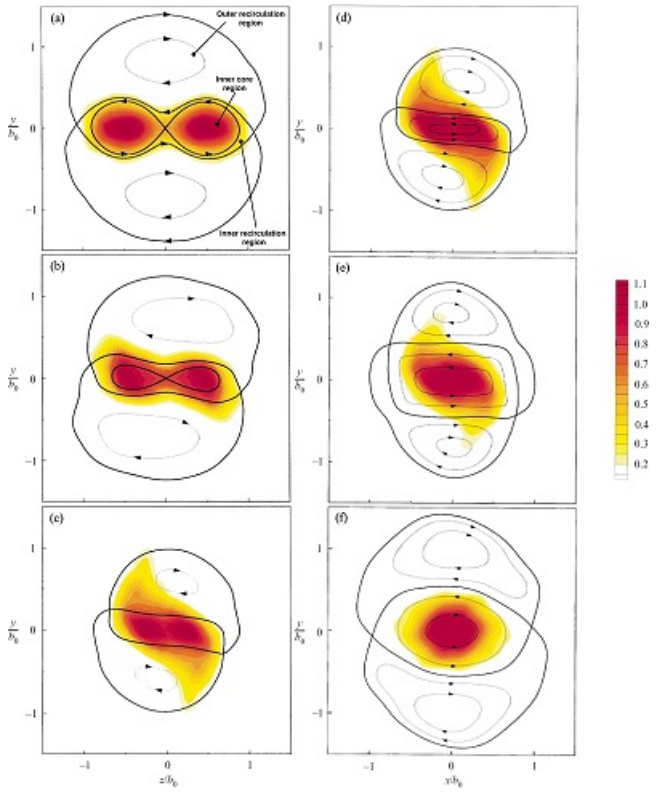

Figure 2.1: The vorticity field of a co-rotating vortex pair superimposed on the separatrices of the co-rotating stream function [8] (the vorticity levels have dimensions of s^{-1}).

vortices spread by viscous diffusion. The core radius increase till a limit value, once it exceeds a critical value a slow evolution of viscous diffusion is modified and the second stage starts. In this phase, the vortices deform and filaments are formed at the edges of the pair. The cores' distance is drastically reduced. The third part of the merging process is a short stage where the separation between the cores tends to zero. Once the process is fully developed, the vortices can be defined as merged; finally, when the distance decreases down to zero, the last phase begins. In this last stage, the final structure develops, the elliptical core becomes axisymmetric and widens.

In order to understand fully the physics behind the merging process, Cerretelli and Williamson [8] have defined three main regions: inner core region, inner recirculation region and outer recirculation region. In the inner core region, the flow rotates with the sense of the vortex. In the inner recirculation region the fluid can travel about both of the cores with the sense shown in the Figure 2.1. While in the outer recirculation, region the flow rotates about the vortices in an opposite sense to that of the cores.

Vortex breakdown is an unsteady process provoked by a dynamic instability. When it takes place, two important consequences have to be highlighted: an abrupt change in the structure of the core swirling flow and a reduction in axial velocity. As Delery suggests [9] the important factor to take into consideration when we have a breakdown is a stagnation point in the centre-line of the structure followed by a reversed flow in a limited area around the axis.

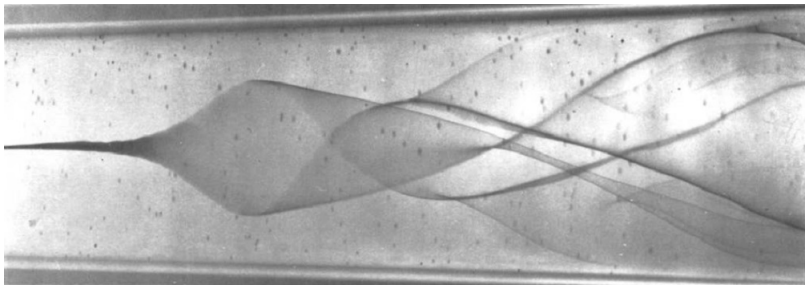

(a) *Double-Helix*

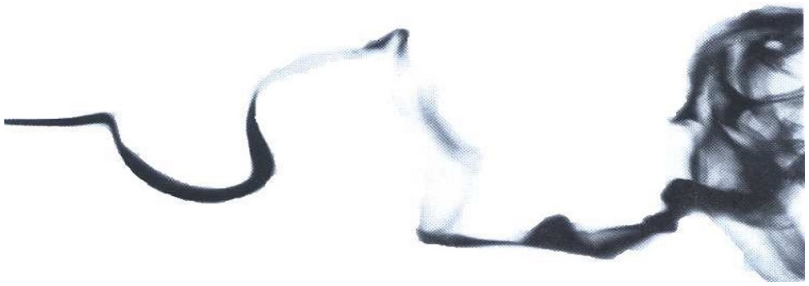

(b) *Spiral breakdown*

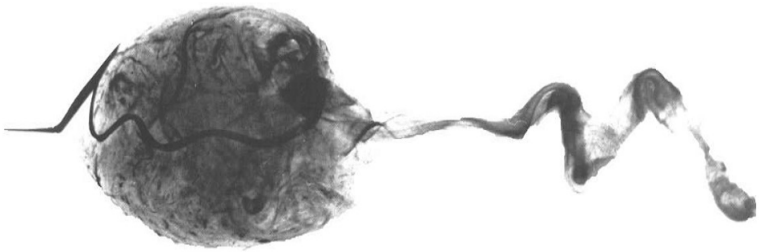

(c) *Bubble breakdown*

Figure 2.2: Flow visualisation of the three main forms of vortex breakdown [11].

By performing dye visualisations of a vortex in water, [10] six main breakdown mechanisms were identified. These, as Sarpkaya suggests [11], are just variations of three main structures named: double-helix, spiral and bubble-type breakdown; they are represented in Figure 2.2. Furthermore Lucca-Negro and O'Doherty [12] offer a wide overview on the various shapes developing during a breakdown; all of them are mainly influenced by the *Re*-number and the swirl intensity of the vortical flow.

2.2 Front Wing in Ground Effect

The front wing of an open wheel car operates in ground effect producing a large amount of downforce due to the airflow between the inverted wing and the ground plane. In particular, low pressure is created underneath the front wing by the effect of the ground plane, which acts almost like the floor of a Venturi's duct. This mechanism therefore, can be applied also to the underbody of cars, thus generating more downforce [2].

A great number of highly complex flow features are associated with the ground effect aerodynamics of race cars. These are identified as flow separation, wall jet, shear layer instability, vortex meandering and breakdown, etc. The vortices for example, which are shed from the endplate, will have a high swirl due to the ground effect, resulting in an increase in suction on the lower surface of the wing. Consequently, vortices shedding from the front wing may be prone to breakdown because of the adverse pressure gradient in which the wing is working, diminishing the axial velocity and therefore decreasing the downforce generated.

Several researches over the last 30 years have investigated the effects of an inverted wing in ground effect [13–16], many of them focused their attention on fundamental aerodynamics instead of practical applications on race cars.

In ground effect as the flow is constrained over the suction surface, an increase in suction thus generating more downforce is expected. The force generated by the wing varies in relation to the ground height. In close proximity to the ground, it was reported that the wing would stall due to the boundary layer separating because of the large suction and the associated pressure gradient. This phenomenon has been investigated by various authors. One of the most complete studies are the ones carried by Zhang and Zerihan [13–16].

Before studying a multiple elements front wing, they performed an investigation on the performance characteristics and flowfield phenomena for a single element wing in a wind tunnel with a moving ground [13]. They focused their attention on the variation of the ride height and angle of attack of the airfoil. As outlined previously, the study highlighted that by diminishing the distance between the ground and the wing, the aerodynamic downforce generated by this device increases. This is true till a threshold they found out to be 10% of the ratio between ride height and chord (h/c); below this value the force decreases due to the separation of the boundary layers generating on both ground and wing. Therefore the study highlighted how the downforce drop was caused by the adverse pressure gradient and not by the boundary layers interaction. Besides, the study underlined that by considering a fixed ground, the aerodynamic forces are underestimated. This is highlighted in Fig. 2.3.

Afterwards, they investigated the effect of the ground on an inverted front wing with multiple elements [15] in a wind tunnel with a moving ground as for the previous study. They found out that it is the main element to generate the most of the downforce produced. Another interesting feature they were able to highlight is that the flowfield has different behaviours depending on the region considered. For example, on the wing centerline the flow can be considered almost bidimensional whereas moving towards the endplate it is more three-dimensional. Furthermore they studied what happens by varying the ride height of the double-element wing, the behaviour is evident in the chart shown in Figure 2.4.

The lift's trend approaching the ground is to increase till a maximum value, before dropping off close to the ground. The graph was split in three different regions for a better description of the phenomena. In region **"a"**, as the ground is approached, the effect of the boundary is to increase the downforce generated by the wing. The latter and the endplate start to act as a diffuser, hence increasing the suction underneath

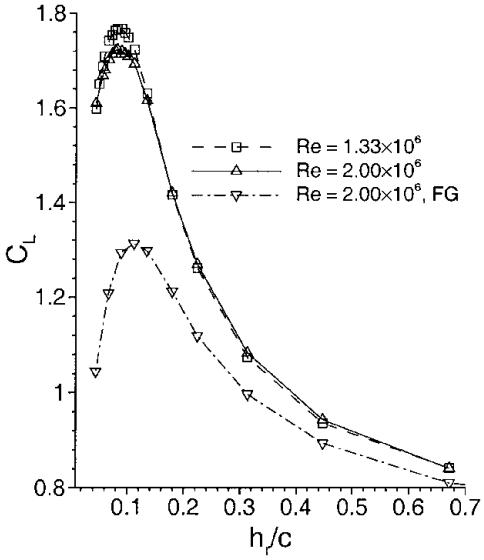

Figure 2.3: Trend of the lift for a single-element wing due to the proximity to the ground [13].

the wing, thereby increasing the lift. Furthermore, it was noticed that as the force increased, the peak of vorticity in the edge vortices was augmented. In region **"b"** the force enhancement continues reaching a peak as a consequence of vortex breakdown. The tip vortices strengthen as the gap to the ground is reduced and the adverse pressure gradient present on the trailing edge of the airfoil increases due to the elevated suction underneath. This mechanism causes the vortices to breakdown as the high swirl in an adverse pressure gradient field cannot be sustained. Hence we can see a drop of the C_L in region **"c"**.

However these researches did not include the wheel presence, which for sure affects the flow physics in this area. A more detailed discussion will be presented in the next section, where the aerodynamics of an exposed racing wheel is described.

2.3 Wheel Aerodynamics

The primary function of the wheels is not aerodynamic; they do not enhance the aerodynamic performance of a vehicle, indeed they are a mechanical necessity with a poor aerodynamic behaviour, especially if exposed to the airflow as for Formula 1 cars. Therefore they are not a profitable area of research when attempting in improving the aerodynamic of a road vehicle.

The open wheels of a Formula 1 car cause much of the complexity in the flow around the car producing strong cross flows in critical areas of the vehicle. They produce about 40% of the total drag [17] and generate lift which is very difficult to capture experimentally. They act like a bluff body, thus generating a large wake which, if not controlled, destroys the underbody's efficiency. They influence particularly the upstream components, front wing and endplate as their trailing edges are extremely close. Therefore it is prudent to do a preliminary understanding of the physics about

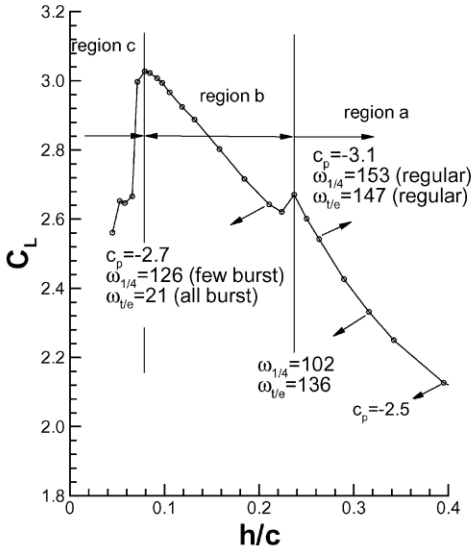

Figure 2.4: Graph of lift augmentation on a double-element wing due to the proximity to the ground taken from Zhang & Zerihan [15].

this subject before leading an investigation of the flow originating from the front wing.

Due to the complexity of this analysis, there are few accepted researches. Some of them are the ones carried by Fackrell and Harvey [18–20]. In their experimental setup that analysed both a stationary and a rotating wheel. They found that the latter leads to a reduction of both lift and drag compared to the stationary case. Also, an earlier separation from the top of the wheel and a less negative base pressure are the results of rotation effects. Fackrell [19] discovered also that when the wheel is rotating, there is a large pressure peak upstream of the contact patch, see in Figure 2.5.

This peak is caused by a phenomenon he called, "jetting", provoked by the moving ground and the tyre which is forcing the fluid towards the contact patch, thus letting it coming out as a jet from the sides of the wheel. Besides, he estimated the separation point of the flow. When the wheel is rotating, the flow separates further upstream than in stationary case, thus reducing the drag for the rotating case. From the image, it is possible to estimate the difference in drag between the two configurations. When the wheel is stationary, around $\theta = 270^\circ$ the base pressure is less than in the rotating case. This leads to a higher drag for the stationary wheel.

Another important feature to be analysed is the wake. Fackrell and Harvey [18–20] showed that the wake is taller when rotating, suggesting and earlier separation as mentioned above. The wake behind the wheel consists of vortical structures, results of the flow over it.

The numerical study of McManus and Zhang [21], which was compared to the experimental time-averaged surface pressure and pressure force measurements by Fackrell and Harvey [18–20], points out some features in the wake, which are highlighted in Fig. 2.6.

Two ground vortices dominate the flow on the road. The vortex nature is evident

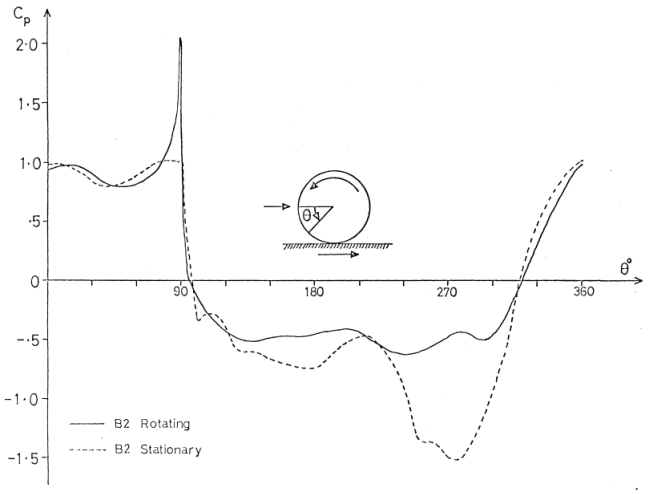

Figure 2.5: Static pressure distribution about both a stationary and rotating wheel as found experimentally by Fackrell [19], (this wheel is referred to as B2 in his experiments).

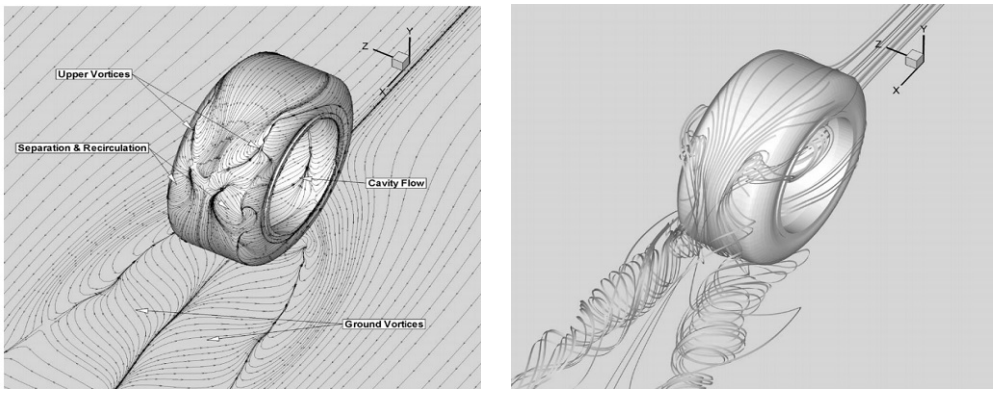

Figure 2.6: Surface flow pattern and volume streamlines on the stationary Fackrell and Harvey geometry [21].

from the volume streamlines and also the surface flow. The surface flow is seen to converge towards two lines and at the centre to diverge from a single line. These lines are called "bipartite" lines. Convergence and divergence around these lines indicate flow separation and attachment. Between these lines, the flow forms an "S-shape" pattern. All of these features are characteristics of a pair of counter-rotating vortices. The left vortex, seen from the rear rotates clockwise, the right one rotates counter-clockwise. On the top of the tyre a complicated surface flow pattern is observed. Two vortices form on the edges and reattach in central area.

Another feature to be discussed is the wake generated by the wheel; previously, it was outlined that in the experiments carried by Fackrell and Harvey [18–20], the separation for the rotating case occurs further upstream than in the stationary case, reducing the drag. This can be misleading and not clear at all. Therefore McManus and Zhang [21] tried to propose an explanation. The real cause of the anomaly is the difference in the oncoming flow conditions. The stationary wheel lies in a boundary layer built up on the stationary ground surface. The flow emerging from under the front

of the stationary wheel is deflected by the low velocity boundary layer flow. In contrast, the flow emerging from under the front of the rotating wheel is deflected by flow with the full freestream velocity. Consequently, the separation region formed around the stationary wheel is deflected less and, therefore, grows larger than in the case for the rotating wheel; thereby explaining the higher drag of the stationary problem.

Other relevant studies are the ones carried by Axerio-Cilies et al. [22, 23]. They conducted computational and experimental studies of a scaled model (60%) of a fixed Formula 1 tyre. They compared experimental PIV data with CFD results from both steady and unsteady simulations (RANS, URANS and LES). As McManus and Zhang found, they highlighted and confirmed the presence of two counter-rotating vortices downstream. The LES were more accurate in replying PIV data, thus allowing to identify better the vortex core and the turbulent eddies and features. Moving far downstream away from the tyre, the differences between steady and unsteady simulations get more negligible.

Pirozzoli et al. [24] have studied the flow around a rolling wheel at low Reynolds number ($Re_D < 1000$, based on the wheel diameter) employing direct numerical simulations (DNS). The study highlighted that the flow around a rolling wheel exhibits the formation of a strong shear layer at the upper edge due to the boundary layer detachment. Increasing the Reynolds number ($Re_D > 400$), the flow becomes unstable yielding a characteristic pattern of hairpin-shaped vortices. The vortex shedding raising the Reynolds number turns to be more chaotic, losing the characteristic symmetric structure for low numbers. However, due to the limited Reynolds numbers simulated, additional structures have been observed. Anyway, this study strongly suggests the importance of using unsteady simulations for a correct prediction of vortex dynamics phenomena.

2.4 Endplate Aerodynamics

As we have seen, generally all the front wings of Formula 1 cars are equipped with a device called endplate. Endplates are one of the most important aspects of the front wing. The optimisation of their position and shape can significantly improve the overall aerodynamics. They control the flow of air around the car by redirecting the airflow around the tyres. This minimises the overall drag resistance and facilitates the airflow to continue back to the side pods and the car floor. The lower to the ground, the better the sealing effect of the endplate and the efficiency of the front wing. However, the height of these devices is regulated by the FIA regulations [3].

This component has assumed different designs along the years. For example curved endplates have been designed in order to ensure that air flows around the tyres. In addition, the endplate stops the high-pressure air on the top of the wing from rolling over to the low-pressure air beneath, causing an induced drag. They may prevent the turbulent air generated by the front wheels to flow under the body of the car, redirecting it outboard. Hence a system of vortices in order to drive the flow around the wheels is generated from this component. A significant feature is the low streamwise speed core of the edge vortex. This is important because the vortex can breakdown easily or

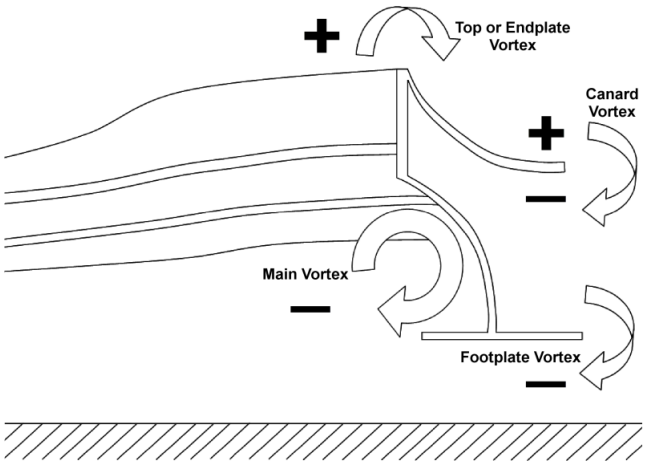

Figure 2.7: A schematic of the topology of the vortex system downstream of the front wing and endplate [25] for this particular shape of the endplate.

dissipate quickly downstream.

Pegrum [25] in his work analysed the vortices flowing from this device. The shape of his endplate let him to identify four vortical structures in the wake, which are visible in Figure 2.7. The most distinct is that located inboard of the endplate. It is called main trailing vortex and it is the wing tip vortex that would be located at the tip if the endplate was not present. The sense of rotation of this structure is found to be consistent with that of a tip of an inverted wing and is clockwise when looking upstream. Consistently this generates an upwash in the wake of a front wing. At the top, another vortex can be identified, named top or endplate vortex. This structure is generated by the pressure difference across the endplate and in his case this vortex strength is enhanced due to the airfoil shaped endplate. The third vortex is generated by the presence of the canard, the device on the outboard side. This vortex is formed due to the shear layer, which develops along the leading edge of the canard. Consistently with the shape of the canard that generates downforce this structure rotates clockwise. The last vortex is located underneath the footplate. This is the reason why it is called footplate vortex; it is formed due to the pressure difference across the plate. The presence of this further component enhances the efficiency of the front wing and endplate by reducing the leakage of the low pressure flow underneath the wing. It also creates a negative pressure on its underside as a consequence of the small ground clearance which causes air to be accelerated beneath it.

As these vortices travel downstream they interact one each other. From the data Pegrum [25] analysed, he found that the main and top vortices were stronger than the other two. Despite the canard and footplate are weaker, their induced velocity is felt by the main vortex. Hence the vortex is displaced upwards as the system travels downstream. This mechanism reduces the separation between the two main vortices. As the system moves downstream the two trajectories resemble that of two unequal co-rotating vortices undergoing the first stages of the merging process.

2.5 Combined Wing and Wheel

As it has been explained in the previous sections, the aerodynamics of the front wing and the wheel has been well studied, since various experimental and computational studies have been done in order to describe the characteristics of the flow around these bodies. Only few studies, on the contrary have investigated the interaction between these two Formula 1 car components. The combination of the two is more complicated to describe and to study since other phenomena and interactions arise.

The first attempt was carried by Kellar et al. [26], who published both an experimental and computational study of the right-hand quarter of a Formula 1 car. In their experiment, they adopted a fixed ground with a rotating wheel, but this was not the best setup since a moving ground gives a better accuracy, therefore their results are quite inaccurate. In the CFD simulation, they modelled a moving ground but with a stationary wheel with a very coarse grid. Due to the unphysical modelling and coarse mesh, it is questionable whether their results represent a realistic flow structure.

One of the most comprehensive studies about this topic was carried by Van den Berg [27] and Van den Berg and Zhang [28], in which a wing is combined with a non deformable wheel similar to a Formula 1 tyre with a camber angle of 2.4° and four longitudinal grooves. The study was both experimental and computational performing different wheel positions and different front wing ride heights.

The experiments consisted of PIV, oil flow, hot wire and static pressure measurements gathering the forces information with load cells placed in different areas. Firstly, it was observed that the wheel drag was dependent on the wing ride height; a lower wheel drag was found in the case of ride height below $h/c = 0.3$ compared to the isolated wing case, and a higher drag for heights above this value. The effect of the wing on the wheel can be explained as a delayed separation over the top of the wheel and by the wake interaction effects.

Compared to the wing isolated case, it was found that the wing in combined configuration produces more downforce for lower ride heights and less at higher ride heights, while the wing drag was found to be generally higher. The wing downforce, as he explains, changes by a combination of the wheel circulation effect due to the wheel rotation, the presence in the downstream flow of the wheel causing obstruction and the damping effect.[1]

In his computations [27], comparing to the simulations of the isolated cases, he found that the results correlated with less accuracy to the experimental studies. A qualitative trend was captured, but the drag prediction in most cases was wrong by more than 25%.

Another reliable study is the one carried by Pegrum [25], which is entirely experimental. He focused his attention more on the tip and endplate front wing interacting with the tyre. As for Van den Berg study [27], firstly he studied both the isolated cases to understand the main features involved, then he tried to analyse and understand what happens in a combined configuration. Considering the nature of his study, as he

[1] *Damping effect: the boundary layer is discharged at the trailing edge into a region of locally higher velocity, reducing the pressure recovery demands, alleviating separation problems or increasing the lift.*

explains, the presence of the wheel introduces a practical difficulty in gathering information upstream, i.e. in front of the wheel. For this reason, the flow information in front of the wheel is quite limited, hence he used the isolated cases as an indication of the likely configuration system to describe the flow.

He noticed that the presence of a rotating wheel generates a region of high pressure upstream of its contact patch, thus changing the strength of the vortices which are trailing from the endplate. These vortices, the main and footplate one, compared to the isolated case behave differently. They rotate about a location that is approximately in the middle of the two structures instead of orbiting about a point close to the strongest vortex. As Pegrum [25] suggests, this may be the result of the interaction with the solid boundaries formed by the inboard edge of the wheel and the ground and the modified strength due to the presence of the wheel. Another explanation he gave is that due to the presence of the wheel, the canard vortex moves differently, thus interacting with the other two structures. The interaction of these two vortices generates a large region of energy losses due to a low total pressure developing in a large region caused by the merging of the vortices cores and by the wheel wake developing downstream. This process generates an high swirling air region where the vortices trailing from the wing merge with the structures developing around the wheel.

Bruckner in his study [29], also tried to give a more detailed comprehension of the effects deriving from a combined configuration, using a numerical approach and PIV additional experiments. In his computations using two different approaches, SRANS with Spalart-Allmaras as turbulence model and DES, he found differences in predicting some main flow features and the drag. Detached Eddy Simulation gave a better precision in drag prediction and a better description of main flow structures.

As Van den Berg [27] and Pegrum [25] suggest, he found that in the combined configuration the wing ride height influences the downforce in a direct way, producing less downforce at high ride heights but more downforce closer to the ground when compared to the isolated case. This is related to the presence of the wheel stagnation point, promoting a higher pressure beneath or above the wing tip. While the wheel rotation does not influence directly the wing downforce at lower ride heights.

The presence of the wheel change also the behaviour of the vortices trailing from the wing. The top edge vortex is diverted upward and inboard by the wheel and has a lower strength compared to the isolated case due to the inboard crossflow developing between the wheel and endplate.

The wheel is sensitive to the presence of the wing too, producing more drag and lift at high wing ride heights. The wing position influences also the flow structure, by introducing sudden changes if moving above or below a certain ride height. For high ride heights he found that the flow around the wheel behaves as an isolated stationary wheel. For low ride heights the flow instead resembles that of an isolated rotating wheel. These changes, as Bruckner says, are associated to the position of the top edge vortex, the circulation induced by the wing and by the lower edge vortex, which undergoes breakdown before reaching the rear wheel. Furthermore, the gap between the endplate and the wheel, as said above, induces a crossflow which increases the separation on the lower front of the inboard tyre shoulder.

Chapter 3

Numerical Setup

This CFD study can be split into three main stages: CAD geometry development, mesh generation and solving stage.

The first section of this chapter gives an overview on the rules followed for the realisation of the CAD geometry and the simplifications adopted. The second part will illustrate the mesh development of the computational domain. The last part will describe the numerical approach used to solve the problem with an insight to the governing equations, the turbulence model exploited, the boundary conditions of the computational domain and the solver setup.

3.1 CAD model design

The geometry developed for this thesis was designed with the support of SolidWorks 2020, a solid modelling computer-aided design (CAD) and computer-aided engineering (CAE) software published by Dassault Systèmes.

The car was designed by respecting the regulations established by FIA for the 2022 Formula 1 Championship. Since the goal of this project is to study the influence of the endplate on the wheel wake behaviour, it was only considered the first right half of the car. The rear part with all his components was not considered in order to achieve the project task.

As highlighted in Sec. 1.2, during the design of the car, some geometrical constraints defined by the FIA 2022 Technical Regulations [3] had to be kept in mind. “Reference Volumes” and “Reference Surfaces” are used throughout the Technical Regulations for geometrical constraints. For convenience, Reference Volumes are preceded by the prefix "RV-" and Reference Surfaces by the prefix "RS-". In Table 3.1 the Reference Volumes, Reference Surfaces and Coordinate Systems considered in this project are listed.

After all these volumes have been drawn and the constraints fixed, the CAD model was developed inside these envelopes. The geometry has a series of simplifications adopted in order to simplify the study of the flow field around the car.

First of all no brakes and suspensions have been considered. Another great simplification has been adopted: all the holes that characterise the wheel have been closed,

Table 3.1: 2022 FIA Formula One Technical Regulations [3].

Parameter	**Acronym**	**Articles**
Nose	RV-CH-NOSE	Art. 3.6.1
Survival Cell Minimum RV	RV-CH-MIN	Art. 3.6.2
Forward Chassis	RV-CH-FRONT	Art. 3.6.2
Mid Chassis	RV-CH-MID	Art. 3.6.3
Front Wing Profiles	RV-FW-PROFILES	Art. 3.9.1
Front Wing Endplate Body	RV-FWEP-BODY	Art. 3.9.2
Front Wing Tip	RV-FW-TIP	Art. 3.9.3
Front Wing Diveplane	RV-FW-DP	Art. 3.9.4
Coordinate Systems	-	Art. 2.9, Art. 2.11, Art. 3.4
Regulation Volumes	RS & RV	Art. A.9, Art. A.10, Art. A.11, Art. A.21, Art. A.22, Art. A.23

such as the ones relative to the wheel rim or the air intake for the brakes. This was done to avoid the complex flow developing in this area.

The geometry is characterised by four main components: chassis, front wing, endplate and tyre, which are shown in Fig. 3.1 with relative bounding boxes. The model studied is full scale.

The front wing is made of three airfoils named in the following way: mainflap element, primary flap and secondary flap. The following configuration have been extruded for 900mm in the spanwise direction, which is the maximum length allowed by the 2022 FIA Formula 1 regulations for the front wing. The shape of the airfoils was not designed following any aerodynamic optimisation rather it was shaped more by looking at the actual airfoils adopted in Formula 1. The chord of the three elements varies along the spanwise direction, thus not being constant. Furthermore the two flaps have been twisted in order to generate downforce; either the primary and secondary elements have zero angle of attack at the root and at the tip sections whereas at the centreline they have incidence respectively of: 16° and 30°. Instead the mainflap has not been twisted, indeed the midspan angle of attack is zero; the same as for the root and the tip sections. Further geometrical details are available in Table 3.2.

The endplate, the winglet at the extreme end of the front wing, is blended to the wing through the tip. Its height with respect to the ground, ride height, is $100mm$. On the outboard of this aerodynamic component, a small device has been designed by looking at the prototypes proposed by the FIA, see Fig. 1.2. This device is called "canard" or in a simple way, "banana" due to its shape. This element will be subject to changes too along this study, in particular its vertical position and angle of attack.

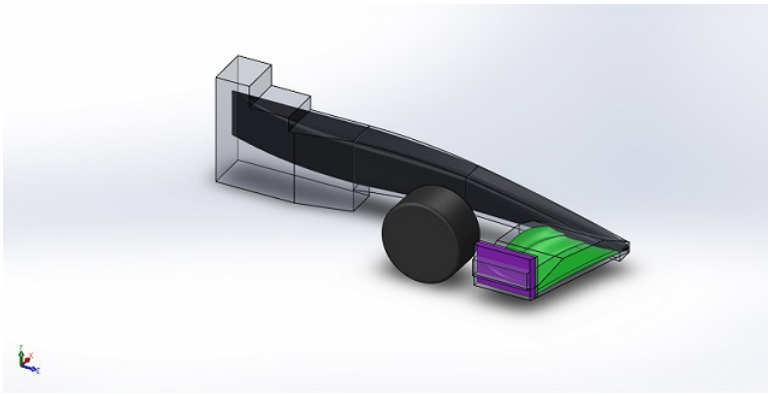

Figure 3.1: CAD geometry of the F1 2022 car generated for the current study with displayed the limiting bounding boxes.

Table 3.2: Front wing measurements.

Parameter	**Mainflap**	**First flap**	**Secondary flap**
Root chord (mm)	269.5	154.72	129
Tip chord (mm)	236.58	141.87	96.23
Mean chord (mm)	253.42	148.39	113.41
AoA ($^\circ$)	0	16	30

In this section, just the dimensions of the first geometry analysed will be provided since it will be used for the mesh independence study and taken as a reference configuration. Further variations will be described later to highlight the differences during the analysis stage. The dimensions of the wingtip and canard regarding the reference configuration are reported in Table 3.3.

The wheel, as said above, is completely closed, the hubs are removed to simplify the geometry and reduce the flow complexity. This greatly simplifies the simulations removing the need to model the wheel spokes with a moving mesh. The diameter is $710mm$ and the fillet radius is $30mm$. It has a camber angle of 2.4° and a contact patch with the ground is considered. The gap between the tyre and endplate, defined as the distance between the trailing edge of the endplate and the foremost point of the wheel, is $120mm$.

3.2 Mesh Generation

The creation of a computational mesh around the model is required to discretise the whole domain of research. The mesh has been developed with the support of Ansys Fluent Meshing [4].

The three dimensional grids created have been developed using the new feature currently present in Fluent. They are based on a Mosaic Meshing Technology called Poly-

Table 3.3: Endplate and canard baseline measurements.

Parameter	**Endplate**	**Canard**
Length (mm)	523	442
Thickness (mm)	15	30
Height (mm)	375	10
Chord (mm)	-	434.17
AoA ($^\circ$)	-	14
Entrance angle ($^\circ$)	-	2
Exit angle ($^\circ$)	-	35

Hexcore. This new technology developed in Ansys allow to generate a high quality surface mesh using polyhedral elements while filling the bulk volume regions with hexahedral elements, which are more computationally efficient and reduce the cell count saving on computational resources without compromising accuracy.

The domain, as explained, represents just half of the car body due to the quasi-two dimensional flow at the centrespan and to reduce the computational mesh size and time.

The domain size adopted is the same for all geometries analysed, with the car body fixed in the same location. The domain extends 1.5 car length (L = $3550mm$) in the upstream direction and $6L$ behind the chassis. The vertical and spanwise size are the same, respectively $1.5L \times 1.5L$, with a square section. The computational domain and its relative dimensions can be seen in Fig. 3.2 and Fig. 3.3.

In order to ensure a better mesh quality around the car, two blocks (i.e. bodies of influence) were generated, allowing for grid refinement and high cell quality in these areas. The first one includes the whole body and extends further downstream to better capture the wake produced. One of the faces is coincident with the symmetry plane. It has a square cross-section of $0.5L \times 0.5L$, while extending $0.5L$ in front of the chassis and $5L$ behind it. The second box was done to get a better and refined mesh around the bodies that generates a more complex flow structure. It has a rectangular cross-section of $0.3L$ of height and $0.4L$ of width, starting from the symmetry plane. The length of this box from the front nose of the chassis is $0.7L$ downstream and $0.1L$ upstream.

A lot of time was spent to ensure a good quality mesh that represented the original geometry and to be considered grid-independent in the sensitivity study. Over all the car surfaces, a boundary layer treatment was given, by developing a series of prism layers. In addition, on the moving ground, prism layers have been developed even though it is moving at the same flow speed and a boundary layer is not expected. This choice can seem a bit improper since a moving ground will not develop any boundary layer; however due to the presence of the car bodies, in proximity of the geometry, the velocity varies, in particular it increases both underneath the chassis and the front wing as explained in Section 2.2 because of the ground effect. Therefore a boundary layer develops in these areas. After many trials, it was seen that a mesh with layers over chassis and ground

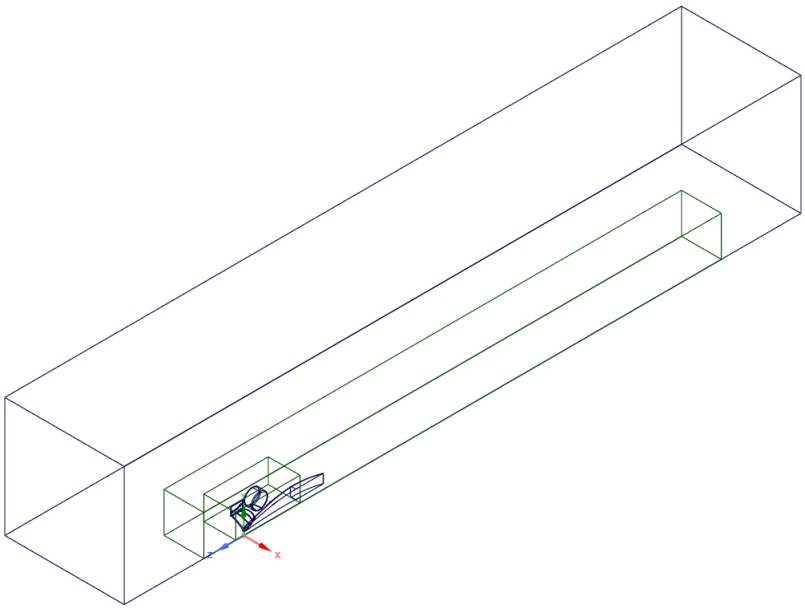

Figure 3.2: Computational domain of the Formula 1 car. In the volume, the bodies of influence around the car are highlighted, these been developed to get a more accurate solution in critical areas.

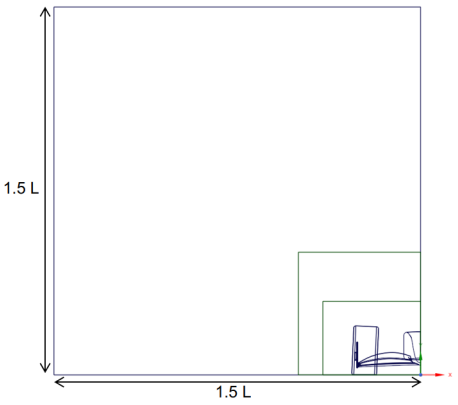

(a) *Front view*

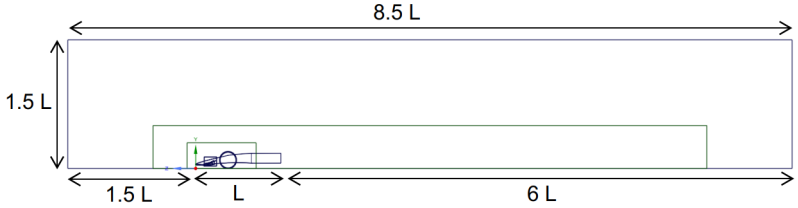

(b) *Side view*

Figure 3.3: Front and side view dimensions of the Formula 1 car computational domain.

gave faster and more stable convergence.

In order to choose the first cell height of the prism layers, i.e. y^+, a briefly consideration should be done.

There are two main approaches regarding the level of details one can reach close to the surface when a turbulent boundary layer is developing: Low Reynolds and High Reynolds. To understand them, it is fundamental to recall the law of the wall, an universal law for turbulent flows in the boundary layer which relates the velocity close to the wall with a dimensionless height, y^+. Depending on the value of y^+, three different regions stand out:

- **Viscous sublayer**: $y^+ < 5$. In the viscous sublayer, the fluid is dominated by the viscous effect, so it can be assumed that the Reynolds shear stress is negligible.
- **Buffer layer**: $5 < y^+ < 30$. The buffer layer is the transition region between the viscosity-dominated region and turbulence-dominated part of the flow. Viscous and turbulent stresses are of similar magnitude and since it is complex, the velocity profile is not well defined.
- **Logarithmic region**: $y^+ > 30$. In the logarithmic layer, turbulent stresses dominate the flow and the velocity profile varies very slowly with a logarithmic function along the distance y.

In a High Reynolds approach the value of y^+ lies in the logarithmic region, meaning the layers developed are not such refined closed to the surface. What happens in the viscous sublayer will not be computed directly but theoretical models will reconstruct the information there by exploiting wall functions. Instead, if the values of y^+ lie in the viscous sublayer, close to the wall a very fine grid has been developed and the viscous quantities will be computed directly while fixing the others in the layers above.

In this work, the turbulence model adopted required an appropriate range of y^+. Since in this study the turbulence model adopted is $\kappa - \omega$ SST, which will be described in Section 3.3.1, the y^+ in these areas was given an average value of $y^+ \approx 30$ thus adopting a High Reynolds approach. This turbulence model allows also for lower values of y^+, but it was chosen not to go below this threshold to avoid a build-up in mesh elements size and computational costs. Therefore prism layers with a growth rate of 1.2 and 15 levels were created. The overall cell skewness has been kept under a certain value (< 0.9) to avoid computational problems. Details of the mesh generated are available in Fig. 3.4.

To investigate the grid sensitivity four grids were tested with increasing number of cells. The total number of cells was 4.8, 5.7, 8.8 and 13.8 million respectively. In Section 4.1 the independence study will be outlined with some charts and the choice of picking one mesh among the others for the remaining analysis will be explained.

3.3 Solving Stage

Once the grid has been generated with Fluent Meshing, the solver setup was defined. In the following section, an overview of the equations used to model the flow and the simulation settings are described.

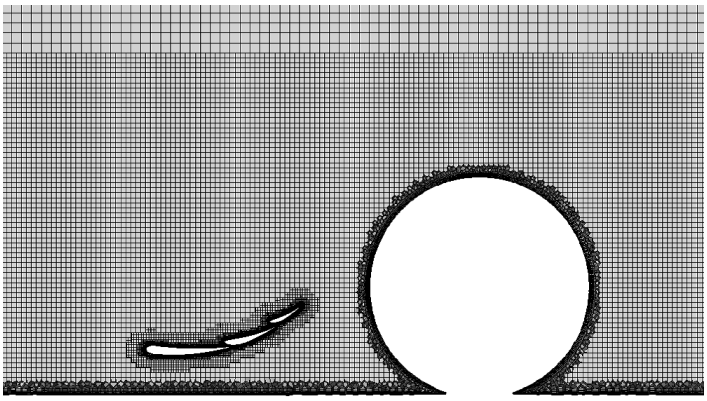

(a) *Side view of a plane cutting wing and tyre*

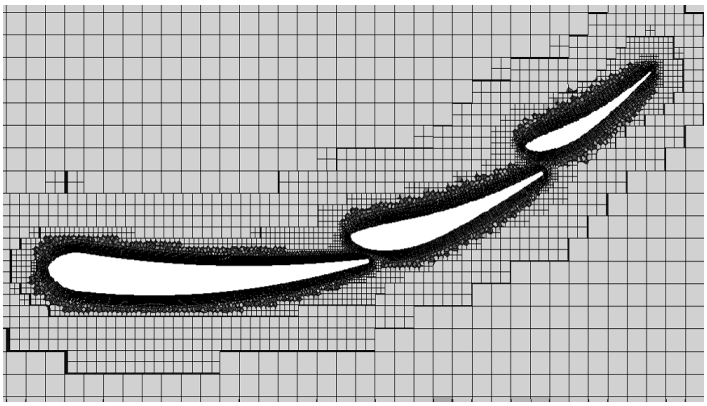

(b) *Side view details of the wing elements*

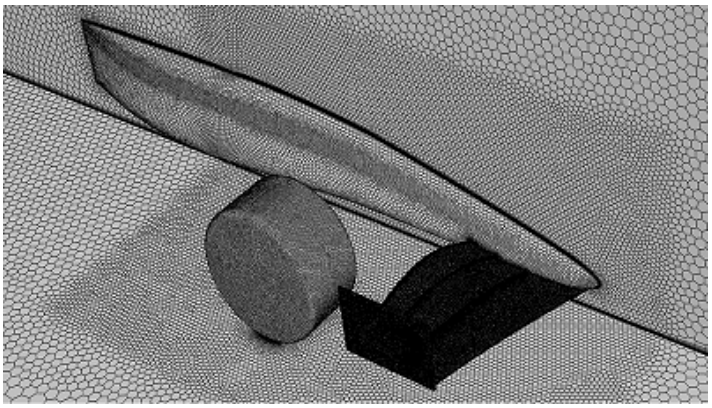

(c) *Surface mesh of the car model, ground and symmetry plane*

Figure 3.4: Details of the mesh developed for this project.

3.3.1 Governing equations and turbulence model

Since in this study, the flow analysed is at relative low Mach number ($M \approx 0.15$), it is considered incompressible. The motion of incompressible fluids can be expressed by the Navier-Stokes equations [30] of continuity and momentum as follows:

$$\frac{\partial u_i}{\partial x_i} = 0 \tag{3.1}$$

$$\frac{\partial u_i}{\partial t} + u_j \frac{\partial u_i}{\partial x_j} = -\frac{1}{\rho}\frac{\partial p}{\partial x_i} + \nu \frac{\partial^2 u_i}{\partial x_j \partial x_j} \tag{3.2}$$

where x_i are the Cartesian coordinates (i = 1; 2; 3), u_i the velocities, p the static pressure whereas ρ and ν are the density and kinematic viscosity respectively and are constant as the flow is assumed incompressible.

Since these equations are non-linear, solving them directly (DNS) is computationally too expensive as the flow becomes more complex due to the complicated geometry. Therefore for problems such this, different approaches that allow to model the turbulence have been developed along the years.

RANS equations

Turbulent flows nowadays are simulated in three main ways: RANS (Reynolds-Averaged Navier-Stokes), LES (Large Eddy Simulation) and DNS (Direct Numerical Simulation). However other approaches exist, they are hybrid, in other words a mix of the ones mentioned previously or based on other assumptions (e.g. LBM). The most famous hybrid approach is the DES (Detached Eddy Simulation), a mix of RANS and DES. Instead, the Lattice Boltzmann method is quite more recent and is an alternative to the common CFD solvers based on the Navier-Stokes equations. This method describes the fluid motion on a mesoscopic scale (i.e. it has both particle and continuos nature), and does not include the non-linearity of the Navier-Stokes equations. One of the advantages is that, complex physics is implemented in a natural way by playing with the details of particle-particle collisions. The simplicity of its formulation allows simpler coding process and it is particularly well suited for parallel computing due to its nature. Particle motion can be easily decomposed on many processor cores or other hardware units. Anyway, this method still has some limitations. At present, high Mach number flows are still difficult to compute and a consistent thermohydrodynamic scheme is absent.

What differs in the three approaches is the way they treat the turbulence spectrum. In RANS all the spectrum is modelled, in LES only the small scales are modelled, the one relative to the dissipative viscous layer while in DNS all the scales are computed without exploiting any model.

In this study, the flow field is modelled following a steady RANS approach since various endplate shapes needs to be compared and the computational power available did not allow to solve all these geometries with an unsteady approach in a reasonable amount of time. However, an overview of both steady and unsteady RANS follows.

Reynolds-Averaged Navier-Stokes are derived directly from the governing equations by decomposing them into the mean and fluctuations components. Velocity and pressure are decomposed in the following way:

$$u_i = U_i + u_i^{'} \tag{3.3}$$

$$p = P + p^{'} \tag{3.4}$$

where U_i and $u_i^{'}$ are the mean and the fluctuation. Therefore substituting the decomposition in the Navier-Stokes equations, we obtain the RANS:

$$\frac{\partial U_i}{\partial x_i} = 0 \tag{3.5}$$

$$\frac{\partial U_i}{\partial t} + U_j \frac{\partial U_i}{\partial x_j} + \frac{\overline{u_i' u_j'}}{\partial x_j} = -\frac{1}{\rho}\frac{\partial P}{\partial x_i} + \nu \frac{\partial^2 U_i}{\partial x_j \partial x_j} \tag{3.6}$$

The variable now is the mean U_i and additional terms appear; $\overline{u_i' u_j'}$ are the Reynolds stresses representing the effects of turbulence. This problem cannot be solved because we have more unknowns than equations (closure problem), hence it needs to be modelled in order to close the equation. In order to close the problem, the Boussinesq hypothesis is introduced. Following this eddy viscosity approach, the Reynolds stresses depend on the mean velocity gradient in the following way:

$$\overline{u_i' u_j'} = \frac{2}{3} k \delta_{ij} - \nu_t \Big(\frac{\partial U_i}{\partial x_j} + \frac{\partial U_j}{\partial x_i} \Big) \tag{3.7}$$

Replacing this hypothesis into the RANS equation one obtains:

$$\frac{\partial U_i}{\partial t} + U_j \frac{\partial U_i}{\partial x_j} = -\frac{1}{\rho}\frac{\partial (P + \frac{2}{3}k)}{\partial x_i} + \nu_{eff} \frac{\partial^2 U_i}{\partial x_j \partial x_j} \tag{3.8}$$

where $\nu_{eff} = \nu + \nu_t$.

Moreover, the partial derivative over time of the mean velocity is not always appearing in the equations. It depends on how it is defined the Reynolds decomposition of the mean value.

We have two possible definitions, the first is a time-mean:

$$U_i = \lim_{T \to \infty} \frac{1}{T} \int_0^T u_i(t) dt \tag{3.9}$$

in this case $\frac{\partial U_i}{\partial t}$ will not appear in the equations and the problem solved is steady (SRANS). Instead if the intention is to solve an unsteady problem, therefore two separated time scales must exist in the flow (T_1 and T_2) and the Reynolds' decomposition of the mean value can be redefined as:

$$U_i = \frac{1}{T}\int_{-T/2}^{T/2} u_i(t+\tau)d\tau \quad T >> T_1 \tag{3.10}$$

therefore the problem solved is unsteady (URANS) with the term $\frac{\partial U_i}{\partial t}$ appearing in the equations.

There are many problems to face when adopting RANS equations. The aim of these equations is to remove unessential information, but during this process a lot of data are lost such as small-scale interactions; hence a lot of important details are missing. When solving problems with RANS, advantages and disadvantages of this approach must be taken into account and a deep analysis to evaluate the results should be considered.

In order to solve the closure problem many turbulence models have been developed; in this study the two-equations $k-\omega$ SST model is adopted and therefore reviewed below.

$k-\omega$ SST

The $k-\omega$ SST turbulence model belongs to the family of two equations turbulence models. It was specifically developed for improved prediction of adverse pressure gradient flows by Menter [31–34]. It is based on the assumption that in an adverse pressure gradient flow, the principal turbulent shear stress obeys the same transport equation as the turbulent kinetic energy. This model is based on a $k-\omega$ formulation, with the original Wilcox [35] model activated in the near wall region and the standard $k-\varepsilon$ model activated in the outer wake region and in free shear layers.

To achieve the desired features in each region Menter developed a blending of $k-\omega$ model in the sublayer with the corresponding $k-\varepsilon$ model for the rest of the flowfield. In order to arrive at a set of equations that can be blended, the $k-\varepsilon$ model is transformed to a $k-\omega$ formulation, introducing additional cross diffusion terms. The original $k-\omega$ model is then multiplied by a blending function F_1 and the transformed $k-\varepsilon$ model by $(1-F_1)$ and the corresponding equations of each model are added together. The blending function is designed to be equal to one near the surface and zero away from the surface. Besides the definition of the eddy viscosity has been modified to account for the transport of the principal turbulent shear stress. As said, the SST model solves two equations, the turbulent kinetic energy equation (k) and the specific turbulence dissipation equation (ω).

Here the complete formulation of the SST model is given:

$$\frac{\partial k}{\partial t} + U_i\frac{\partial k}{\partial x_i} = \frac{\partial}{\partial x_j}\Big[\Big(\nu + \frac{\nu_t}{\sigma_k}\Big)\frac{\partial k}{\partial x_i}\Big] + P_k - C_\mu \omega k \tag{3.11}$$

$$\frac{\partial \omega}{\partial t} + U_i\frac{\partial \omega}{\partial x_i} = \frac{\partial}{\partial x_j}\Big[\Big(\nu + \frac{\nu_t}{\sigma_\omega}\Big)\frac{\partial \omega}{\partial x_i}\Big] + \gamma\frac{\omega}{k}P_k - \beta\omega^2 + (1-F_1)\frac{2\sigma_\omega}{\omega}\frac{\partial k}{\partial x_i}\frac{\partial \omega}{\partial x_i} \tag{3.12}$$

where the blending function F_1 is defined as:

$$F_1 = tanh(arg_1^4) \tag{3.13}$$

$$arg_1 = min\Big[max\Big(\frac{\sqrt{k}}{C_\mu \omega y}, \frac{500\nu}{y^2\omega}\Big), \frac{4\rho\sigma_{\omega 2}k}{CD_{k\omega}y^2}\Big] \tag{3.14}$$

The blending function is equal to zero away from the surface ($k-\varepsilon$ model), and switches over to one inside the boundary layer ($k-\omega$ model).

The turbulent eddy viscosity is defined as follows:

$$\nu_t = \frac{a_1 k}{max(a_1\omega, \Omega F_2)} \tag{3.15}$$

where Ω is the invariant measure of the strain rate and F_2 is a second blending function defined as:

$$F_2 = tanh(arg_2^2) \tag{3.16}$$

$$arg_2 = max\Big(2\frac{\sqrt{k}}{0.09\omega y}, \frac{500\nu}{y^2\omega}\Big) \tag{3.17}$$

The SST model, as Menter suggests [31–34], leads to a significant improvement for all flows involving adverse pressure gradients and should be the model of choice for aerodynamic applications. It is the only available two-equation model that has demonstrated the ability to accurately predict pressure-induced separation and the resulting viscous-inviscid interaction.

3.3.2 Boundary conditions

To ensure a good representation of the reality and aiming to an optimal configuration, it was important to set the right boundary conditions at the different interfaces (Table 3.4). First of all, a symmetry condition was imposed in the symmetry plane, which assumes a zero flux across it of all the quantities. The top and lateral sides were defined as symmetry conditions too, to avoid a high grid density required to solve the boundary layer if these were considered walls. Besides, the symmetry condition was also useful to reduce the mesh size by half, dropping the computational cost of the simulations.

The upstream interface was defined as a velocity inlet with a normal velocity of $50 m/s$, which corresponds to a chord-based Reynolds Number of 1.82×10^6. The turbulent viscosity ratio and the turbulence intensity were chosen similar to Bruckner [29] and Van den Berg [27] studies, respectively their values have been set to 1×10^{-7} and 0.3%. The downstream boundary was set as a pressure outlet with a gauge pressure of 0, with the same parameters of the inlet. The air density and the dynamic viscosity were fixed to constant values ($\rho = 1.225 kg/m^3$ and $\mu = 1.7895 Pa/s$) as the flow is considered incompressible.

Table 3.4: Boundary conditions employed in the simulations.

Surface	**Boundary condition**
Inlet	Velocity Inlet
Outlet	Pressure Outlet
Ground	No-Slip Moving Wall
Front Wing	No-Slip stationary wall
Chassis	No-Slip stationary wall
Symmetry Plane	Symmetry
Top Wall	Symmetry
Far Wall	Symmetry
Wheel	Rotating No-Slip wall

The bottom of the domain, or rather the ground, was defined as a no-slip moving wall with a velocity equivalent to the freestream both in magnitude (i.e. $50m/s$) and direction. The front wing (i.e. the three airfoils and the endplate) is a no-slip wall, as well as the chassis. The wheel instead was defined as a rotating wall. The angular velocity about its rotational axis is $140.85rad/s$, based on the ground velocity and the wheel radius.

3.3.3 Solver setup

This project has been developed by exploiting a workstation provided by the Universidade da Beira Interior (UBI). The CPU is made of 8 processors (16 logical), Intel Core i9-9900K with a maximum frequency (clock rate) of 3.6 GHz. The memory (RAM) is an important factor for this case and more in general for three-dimensional meshes or high elements grids. Therefore depending on the number of cells more or less memory was used by the software while running. The maximum amount available was of 64 GB.

A pressure based solver exploiting the implicit segregated algorithm with a least square gradient method was used to solve all the simulations. As explained above, a steady RANS approach was adopted in this work. To interpolate the variables (u_i, κ and ω), a second order upwind method was chosen and for the pressure a second order scheme. The SIMPLE (Semi-Implicit Method for Pressure-Linked Equations) algorithm has been selected for the pressure-velocity coupling.

The solution was initialised with a standard initialisation, setting constant values from the inlet and then running a Full Multigrid (FMG) initialisation from the TUI (Text User Interface) command. This kind of process gave a faster and better convergence since the flowfield was initialised better. FMG is computationally inexpensive and fast. Euler equations are solved with a first order accuracy on the coarse level meshes. FMG uses the Full Approximation Storage (FAS) multigrid method to solve the flow problem

on a sequence of coarser meshes, before transferring the solution onto the actual mesh.

In order to reach a good and reasonable solution and results, a certain level of residuals and force coefficient should be obtained. That is why a convergence criterion was set firstly to $1e^{-3}$ for the continuity residual, which is a reasonable value for this kind of problem; whereas the aerodynamic coefficients concerning the front wing have been monitored till they behaved in a stable way. Nevertheless for flow cases involving bluff bodies and large separated zones like for this project, these criteria should not be applied straightforwardly since residuals and force coefficients could be oscillating irregularly. In this study all the simulations reached the residual criterion, however the force coefficients keep on oscillating between an upper and lower limit. Hence, to determine and fix the values, a mean has been evaluated after the simulations converged and stabilised around a range band. This coefficients behaviour is related to the physics of the problem which is typically unsteady. Hence, considering a steady solution of the problem, it is reasonable to expect this trend. The behaviour is emphasised as well by a relative low Reynolds number and a not enough dissipative discretisation method.

After many trials, the relaxation factors of momentum and pressure were set to 0.3, while for the two equation of the turbulence model they were set to 0.5. These values gave a smooth convergence without a lot of oscillations in a reasonable amount of time.

3.4 Validation of Numerical Setup

The numerical method which has been set up and then used need to be validated. Since the problem analysed in this project is about the new regulations of the next Formula 1 championship [3], no studies to compare with are available. Furthermore, the previous studies discussed in Chapter 2 are simpler or referring to other norms. Therefore there is no way to compare directly the results obtained in this study. Hence, it has been chosen to validate the numerical setup looking at a certain parameter of an airfoil (e.g. C_P) and comparing it with experimental data or some software as Xfoil [36] or XFLR5 [37].

To have the most accurate validation, the same inlet velocity, chord and Reynolds number of the main element of the front wing should be exploited; no experimental data have been found in literature regarding any airfoil study with any of these settings. So it has been decided to carry on a validation comparing just with XFLR5.

This software is an analysis tool for airfoils, wings and planes. It includes XFoil direct and inverse analysis capabilities based on the lifting line theory, on the vortex lattice method and on a 3D panel method. For this reason, the results coming from a CFD simulation may not have the same exact behaviour due to a difference in the solving method. Anyway, these methods give an accurate solution very close to the reality, so they are suitable for a comparison with a CFD code.

The airfoil taken into consideration is a NACA 2214, with a chord of $250mm$ and a width in the spanwise direction of $900mm$, same of the main element of the front wing. To avoid three-dimensional effects on the wing tips, symmetry conditions have been set laterally, above and below the airfoil. The inlet and outlet have the same boundary conditions of the car computational domain. Therefore the air behaves in a

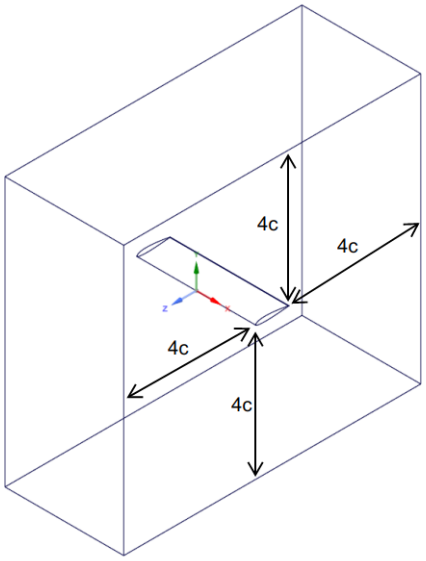

Figure 3.5: NACA 2214 computational domain and relative dimensions.

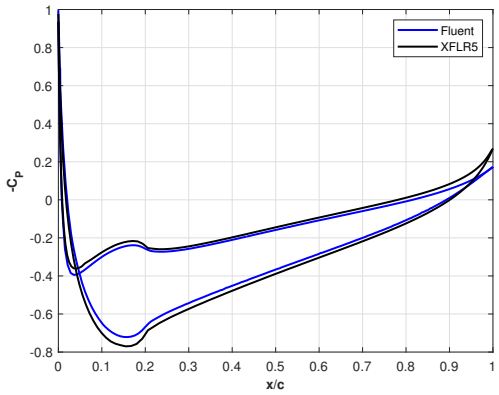

Figure 3.6: C_P comparison between the CFD simulation run in Fluent and XFLR5.

two-dimensional way especially on the midspan which has been taken as reference plane to analyse the pressure coefficient. The computational domain has been extended for four chords ($4c$) upstream, downstream, above and below the NACA 2214, as shown in Fig. 3.5. To validate, the same numerical setup (i.e. numerical methods, discretisation, relaxation factors and turbulence model) of the project have been taken.

The result (available in Fig. 3.6) is quite good since the trend of the C_P from the CFD simulation replies relatively faithfully the one from XFLR5. The discrepancies between the two graphs may be related, as explained before, to the different methods used in solving the problem. Anyway, the chart obtained allow to assert that the numerical method used in this project is correct and therefore validated.

Chapter 4

Results

In this chapter, after having developed the mesh and validated the numerical method, different configurations of the endplate will be analysed comparing them with respect to the reference baseline geometry chosen.

The chapter is split into two main sections: firstly, the grid independence study will be shown in order to justify which one of the four grids have been picked to carry on the analysis. Afterwards, the analysis and physical discussion, highlighting the vortical structures and total energy losses, will be reported.

The post-processing is mainly achieved by using the inside tool present in Fluent and the commercial software Matlab.

4.1 Grid Sensitivity Study

When dealing with CFD, it is recommended before proceeding with the analysis of a certain solution to conduct a grid sensitivity study in order to prove that the solution is grid independent, thus not changing with the number of cells in the computational domain. Anyway, it is not always possible to reach mesh independency and if reached it does not ensure a good quality of the results; however, a good amount of time and resources need to be spent in order to try reaching this task. For this project, a lot of time was spent to ensure convergence and grid independence. Regarding this last task no clear independence has been reached; however, the mesh which gave a good compromise between results and computational time was picked and later used to carry on the remaining goals of this project.

As previously mentioned in Sec. 3.2, four different grids have been generated, respectively with 4.8, 5.7, 8.8 and 13.8 million cells. The parameters which have been monitored for this study are the aerodynamic force coefficients of the front wing (i.e. C_L and C_D).

The grids generated do not show great variations, anyway an independence behaviour is not clear. This is well explained by looking at Fig. 4.1. Indeed, it is possible to point out that, as increasing the number of cells elements, there is no big difference between the four grids regarding the force coefficient values. In Table 4.1, the relative errors of

Table 4.1: Grid sensitivity relative errors w.r.t. to Mesh 4 (13.8 Mln cells).

	Number of cells (Mln)	$C_{L_{err}}$	$C_{D_{err}}$
Mesh 1	4.8	0.76%	0.51%
Mesh 2	5.7	0.39%	0.96%
Mesh 3	8.8	0.23%	0.17%
Mesh 4	13.8	-	-

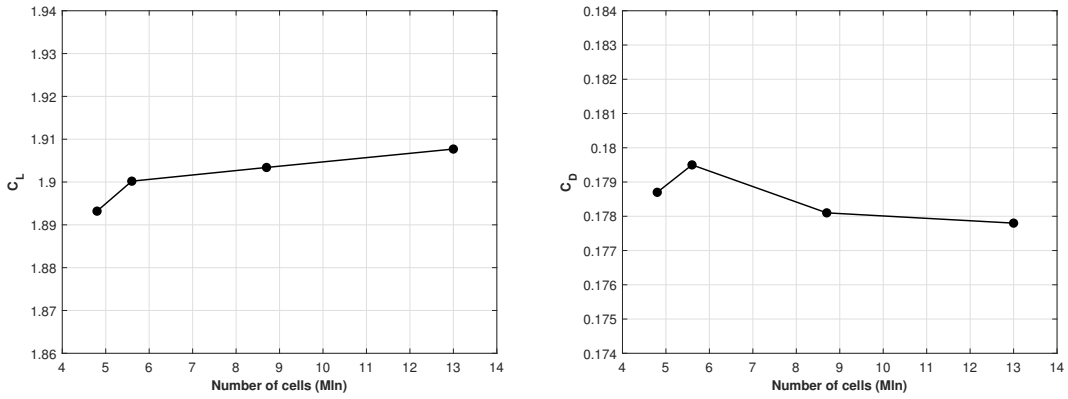

(a) C_L *grid sensitivity* **(b)** C_D *grid sensitivity*

Figure 4.1: Grid sensitivity study of the four meshes respectively with 4.8, 5.7, 8.8 and 13.8 million cells.

the grids compared to the finest one are reported.

If the C_L shows a monotonic behaviour, the C_D shows a bump for the second mesh that highlights how the mesh developed is not entirely independent. For this reason the second mesh is not taken into consideration since the C_D is higher. One can say that it is fine to pick the first grid, which is smaller and thus not expensive in terms of computational costs. However other considerations need to be done. The coarsest mesh could give good results, but, since the volumes around the car are not so refined, some features may not be highlighted and described well. It is rather better to pick the third grid (8.8 million cells) because a more refined mesh captures in a better way the physics phenomena developing around the car's bodies (e.g. vortices, separation zones, etc.). Therefore, the third mesh has been chosen since it is a right compromise between computational costs and solution accuracy.

4.2 Flow Analysis

This section will focus on the goal of this thesis by analysing and discussing the flow features that an endplate geometry variation generates. The main objective is to study and highlight how these variations influence the wheel wake behaviour in terms of energy

losses.

Four main analysis have been carried. The first one deals with the canard location on the y-direction, the second investigates the angle of attack of the canard, the third aims to understand which difference is produced varying the side shape of the endplate and the latter studies what happens by adding a footplate of different dimensions to the endplate. Each comparison will focus onto two main topics: the flow analysis around the wing and the wheel.

The main goal of a Formula 1 front wing is to generate downforce, as already widely explained. However in addition, this component has another purpose, to shape the flow around the car, impacting significantly the downstream objects. Furthermore on the tip, a winglet is present, its goal is to drastically increase the efficiency by reducing the drag. A trailing vortex system travelling downstream about the rotating wheel, is generated by the front wing and endplate. These vortices play an important role, especially the lower edge vortex, being one of the downforce enhancement mechanisms.

The second topic focuses on the wheels, which are strongly affected by the flow coming and by the front wing and endplate configurations. As explained in Sec. 2.3, the wheels are critical components in the development and study of a Formula 1 car, by generating a lot of drag and creating a chaotic flowfield. Therefore it is important to understand the evolution of the flow around them in order to be able to control it, since they influence the feeding process of the underbody due to their proximity to the chassis. For one of the analysis, attention will be paid also to the forces on the wing since the addition of a component greatly improves the efficiency of the front wing.

Various parameters will be taken into considerations to carry on this analysis, such as total pressure coefficient (C_pT)[1], velocity components, non-dimensional z-vorticity and a vortex identification method (Q-criterion) will be employed in order to visualise the flow structure and topology, for the most significant tests.

In Formula 1, the observation of the C_pT is a common process when examining such complex flow structures. This is a non-dimensional parameter that translates the energy of the flow relative to the car. It is defined as:

$$C_pT = \frac{p_t}{p_{t_0}} \tag{4.1}$$

where p_t is the total pressure in any point and p_{t_0} is the total reference pressure, that for this work has been taken at the inlet. The red areas indicate high energy flow, while the blue areas reveal low energy flow, making it possible to extract some information about how effective the components will be and where there is still high energy flow to play with. The images obtained from CFD regarding C_pT can also give an idea about the presence of vortical structures. The aim is to understand which geometry gives a better behaviour in the tyre wake in terms of energy losses.

[1] *The total pressure [38], also known as stagnation pressure, is the pressure at a stagnation point when the velocity reduces to zero. In a practical way it is obtained from a Pitot tube which in turn, for an incompressible flow, allows the calculation of the velocity via the Bernoulli's equation if combined to a static probe. The total pressure is computed as:* $p_t = p_{static} + \frac{1}{2}\rho V^2$*, where the second term represents the dynamic pressure.*

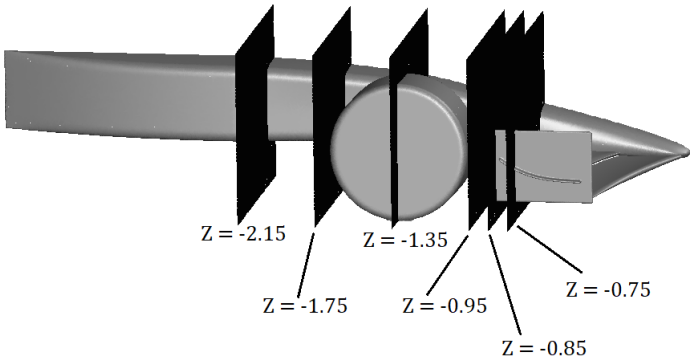

Figure 4.2: Locations of the planes generated in the z-direction to access the flow field during the analysis.

It is important to underline that in this study, since a steady formulation has been carried on for the reasons explained in Sec. 3.3, a lot of information and details will be lost due to the unsteady nature of the phenomena developing around these objects. Unfortunately no experimental studies are available for a direct comparison of these project results. Therefore it is more complicated to understand how far or close SRANS simulations are in predicting the exact flow features. Anyway various works have been useful to understand the quality of the results obtained.

Since a grid sensitivity study has already been performed for the reference configuration, it has been skipped for the remaining configurations in order to save computational time.

To access and analyse the flowfield, several measurement planes will be considered as shown in Fig. 4.2. These planes have been placed in areas of interest in the streamwise direction in order to reach the project goal.

4.2.1 Canard location analysis

In this analysis, the reference configuration will be compared with two different endplate layouts. The position of the canard will be changed by moving this component up and down of $10mm$ in the y-direction by respecting the dimensions limits imposed by the FIA. The aim is to understand what happens to the flow around the wing and especially in the wheel wake by imposing these changes.

Wing

Analysing the C_pT (showed in Fig. 4.3), it is possible to identify a system of three vortices developing around the endplate, respectively lower edge vortex, canard vortex and top edge vortex. Both of them rotating in an anti-clockwise direction if seen from upstream. The formation of these structures is caused by the pressure difference and by the boundary layer separation on the edges moving from higher pressure zones to lower.

As they travel downstream, approaching the wheel, they gain energy. No substantial differences can be found within the three geometries. The only thing to be highlighted is that the canard vortex is slightly upwards or downwards as one would expect depending on the canard position. In terms of pressure losses there are no differences between the three configurations regarding the flow crossing the wing.

Observing Fig. 4.3, it is possible to understand the evolution difference of these structures. The lower edge vortex gets significantly larger as the flow develops towards the wheel, whereas the other two stay relatively small. This latter vortex is prone to burst and breakdown due to the great losses in the vortex core, which do not allow to get through the adverse pressure gradient right behind the wing. Indeed the streamwise speed core is very low, even flowing in the reverse direction which is a feature of vortex breakdown [9]. This structure flowing downstream dilates, losing energy and worsening the downforce enhancement mechanism underneath the wing.

Wheel

The wheel wake can be split into two main regions: upper wake and lower wake. The latter extends further downstream due to the ground presence and the jetting phenomenon.

At plane $z = -1.35$ in Fig. 4.4, it is possible to observe that in all three configurations, in the lower region, the turbulent flow is more confined. Two vortices are well defined, both of them results from the jetting phenomenon explained previously in Sec. 2.3. The inboard vortex, which is bigger than the smaller outboard one, results from the summation of the lower edge vortex shedding from the front wing and jetting phenomenon. Even though the turbulence here is confined, the two vortices are prone to breakdown; in particular the inboard one, since low energy is exhibited in its core resulting in a very low and even reverse streamwise speed core. In the following planes $z = -1.75$ and $z = -2.15$ downstream of the wheel, the large region of energy loss observed in the total pressure distribution is associated with a large region of swirling air. The wake is about the same size for the three configurations, however less losses are present in the downwards layout, thus leaving more fluid available for the feeding process of the underbody.

For all of them, at plane $z = -1.75$, it is possible to observe in Fig. 4.5 clearly two vortices; these are a pair of counter-rotating vortices shedding from the tyre shoulders. Their strength may be correlated to the position of the canard vortex, indeed the outboard one is affected by the canard position; the upper the dive plate is, the greater the pressure losses are but in a confined region. The explanation for this phenomenon can be related to the position of the canard vortex. An upper canard vortex may interact more with the top edge vortex and the tyre shoulder, thus favouring its formation or merging.

Regarding the two top edge wheel eddies, since they are rotating in opposite directions, as it is shown in Fig. 4.5, the velocities in the midspan wheel profile sum up, thus pushing the air towards the ground. Depending on their relative strength, the wake will be shifted inboard or outboard. On the lower wake region, a pair of other two counter-rotating vortices should be present, as we have seen for the isolated wheel in Sec. 2.3.

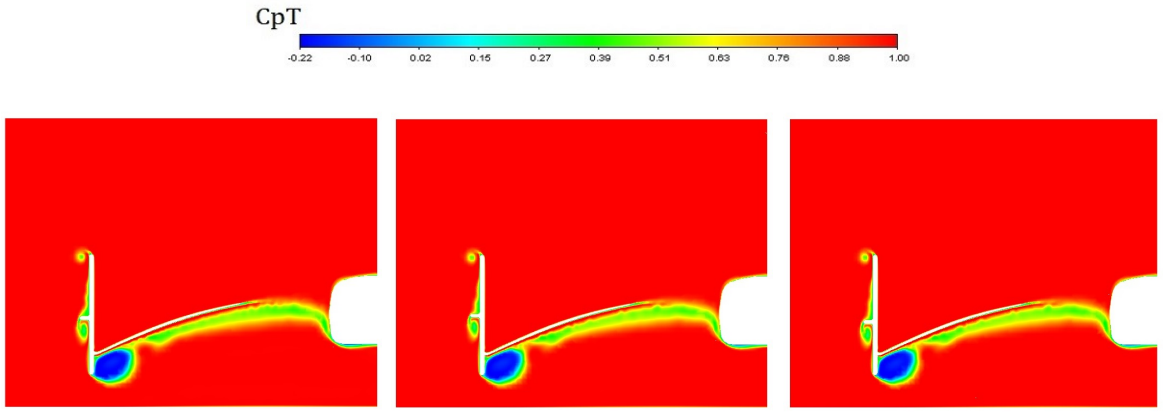

(a) *Plane* $z = -0.75$

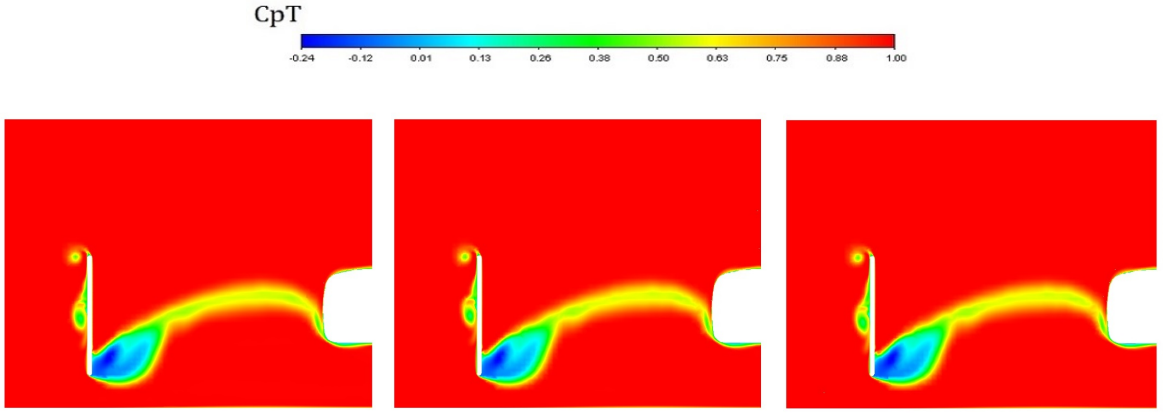

(b) *Plane* $z = -0.85$

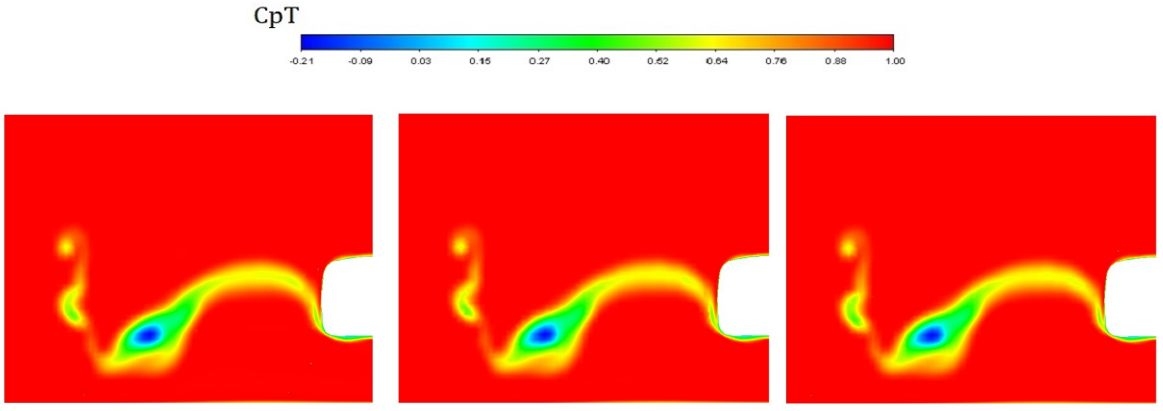

(c) *Plane* $z = -0.95$

Figure 4.3: Total pressure coefficient upstream of the wheel for canard in different positions. It is possible to observe how the three vortices evolve towards the three planes for the three different configurations. From the left: baseline layout, upwards canard and downwards canard.

Table 4.2: Wheel aerodynamic coefficients for the first configuration set.

	$C_{L_{wheel}}$	$C_{D_{wheel}}$
Reference layout	0.3631	0.3760
Upwards canard	+2.45%	−0.08%
Downwards canard	−1.79%	−4.71%

Their presence is affected by the components upstream, i.e. front wing and endplate, in particular the presence of the inboard vortex on the wheel side, generates interactions with the flow in the lower wake region. This process can lead to a merging process of this vortex with the whole wake as it happens for the baseline configuration. Where it is not possible to distinguish the inboard wheel vortex from the swirling region behind the wheel profile.

For a better understanding of the wheel wake, streamwise (Fig. 4.6) and vertical (Fig. 4.7) velocities will be shown. These parameters offer a better overview of what is happening in the wake zone. The streamwise velocity displays the velocity deficit caused by the reduced dynamic pressure in the wheel wake, while the vertical shows the change in flow angle, where zero is aligned with the freestream flow, positive is upwash and negative is downwash.

Concerning the streamwise velocity, at plane $z = -1.75$, the wake between the three geometries shows a similar behaviour with quite strong reversed flow especially for the first two, in particular in the lower wake region. Further downstream at plane $z = -2.15$, similar behaviour is shown again. The downwards configuration has less reversed flow with a more confined wake in the lower area. For the vertical velocity (Fig. 4.7), at plane $z = -1.75$, the downwards layout, unlike the other two, shows a smaller area of downwash especially in the lower wake region right behind the wheel centreline. This is coherent with what has been shown in the vorticity images (Fig. 4.5). The bigger region of vorticity in the first and second configurations generates more downwash in the wheel profile. At plane $z = -2.15$, the wake behaviour is about the same. A big region of upwash is identified in the chassis proximity whereas a small region of downwash is identified behind the wheel.

Since till this point, a qualitative analysis of the wake has been given for the different canard positions and its changes highlighted, a briefly description of how the tyre loads change can justify and complete the previous description. In Table 4.2, the wheel aerodynamic coefficients are reported.

An higher value of the $C_{L_{wheel}}$ means that the wheel has less grip. Despite having represented in Sec. 4.1 the wing lift coefficient with a positive value, considering our reference system it is negative (i.e representing the downforce), hence the values displayed in this table, which are positive, represent the lift. This is consistent with the rotating wheel simulated in our problem. The downwards canard shows a better behaviour as suggested previously, thus showing less lift which can be interpreted with more grip on track and also less drag.

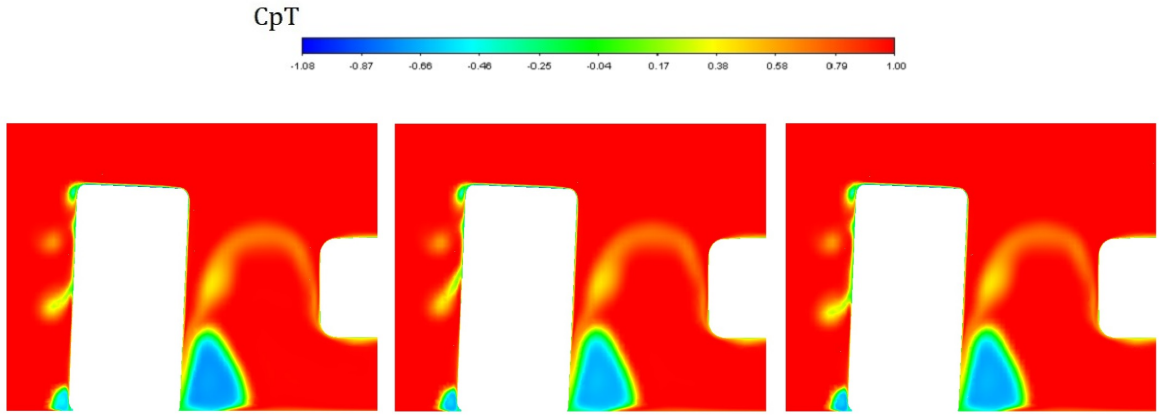

(a) *Plane* $z = -1.35$

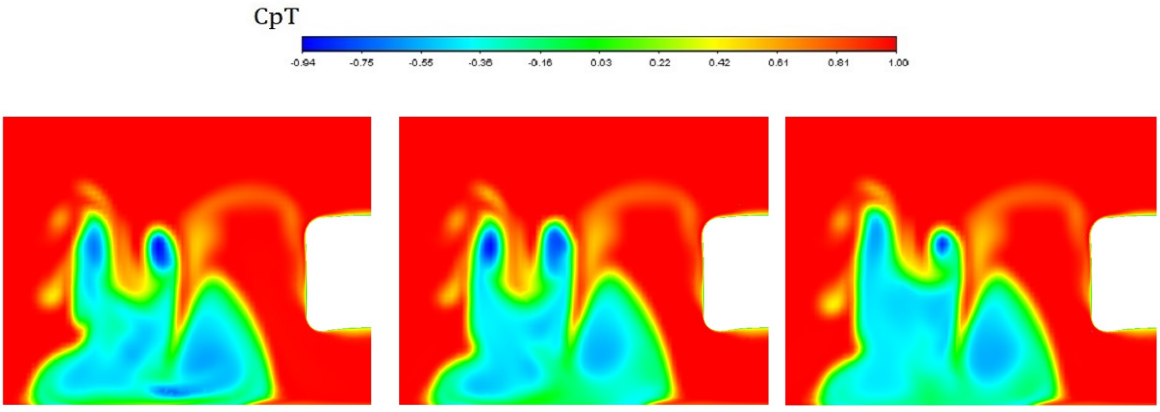

(b) *Plane* $z = -1.75$

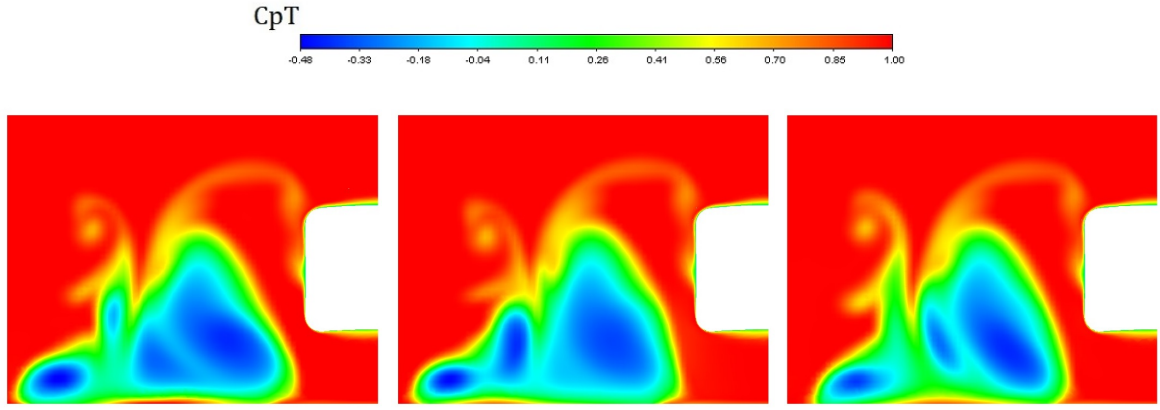

(c) *Plane* $z = -2.15$

Figure 4.4: Total pressure coefficient downstream of the wheel for canard in different positions. It is possible to observe how the wake evolves towards the three planes for the three different configurations. From the left: baseline layout, upwards canard and downwards canard.

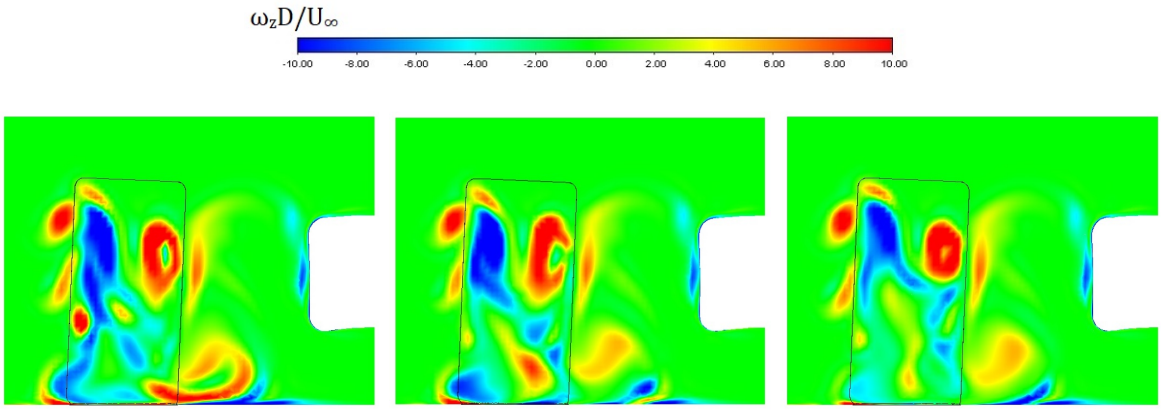

(a) *Plane* $z = -1.75$

Figure 4.5: Non-dimensional vorticity contours at plane $z = -1.75$ for the three canard locations. From the left: baseline layout, upwards canard and downwards canard.

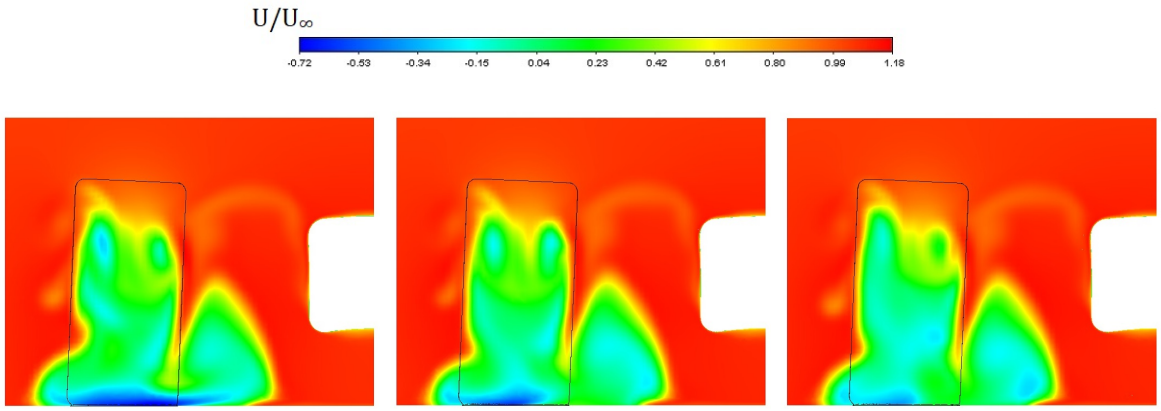

(a) *Plane* $z = -1.75$

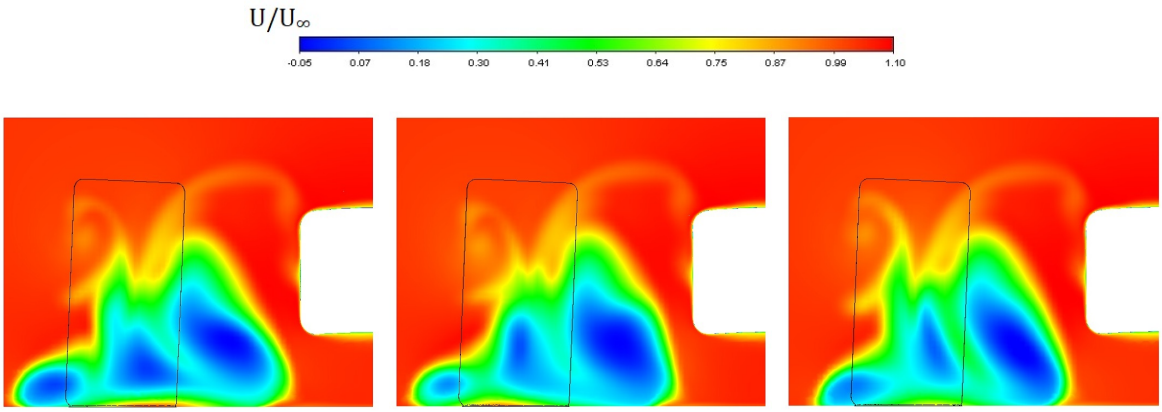

(b) *Plane* $z = -2.15$

Figure 4.6: Streamwise velocity in the wheel wake for canard in different positions. From the left: baseline layout, upwards canard and downwards canard.

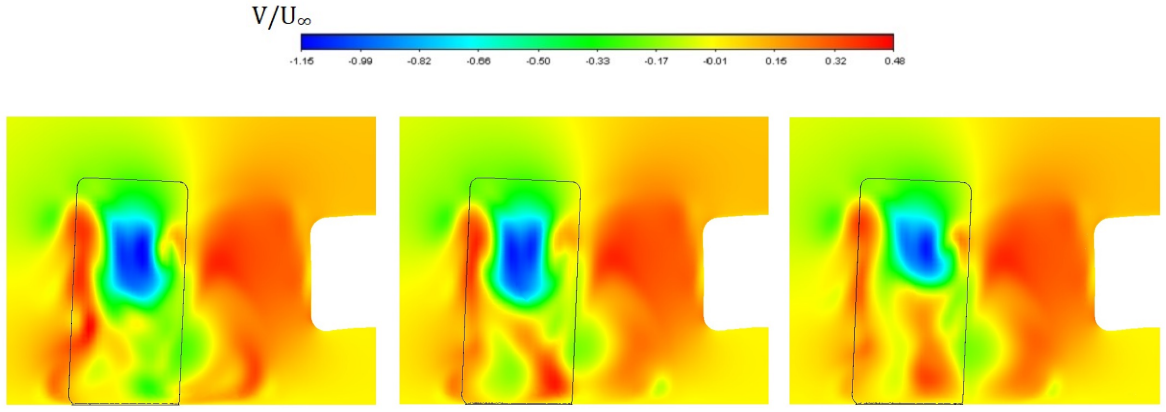

(a) *Plane* $z = -1.75$

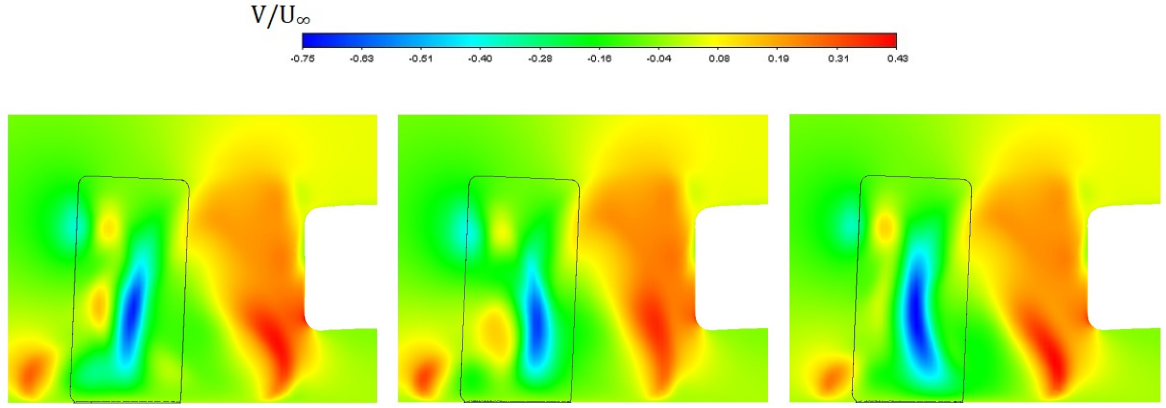

(b) *Plane* $z = -2.15$

Figure 4.7: Vertical velocity in the wheel wake for canard in different positions. From the left: baseline layout, upwards canard and downwards canard.

4.2.2 Canard angle of attack analysis

In this section, the reference configuration will be compared with other two geometries. The component under analysis will be again the canard but for this case with two different angle of attack with respect to the streamwise direction. The rotation will be respectively of 2° and 4° around the leading edge thus increasing the angle of attack of the canard.

Regarding the wing structure no big differences can be found between the three layouts and therefore it has been chosen not to present any result regarding the upstream flow. The only slight discrepancy is in the canard vortex which is imperceptibly upwards for both the two configurations taken into consideration. However this difference does not create any changes in the wing flow structure which is very similar to the one analysed in the previous section.

Wheel

Even though not showing huge discrepancies, the C_pT shows more interesting features than for the wing flow. In Fig. 4.8 starting from plane $z = -1.35$ it is possible to find some diversities. In the reference configuration it is well defined an area of pressure losses on the outboard side of the wheel at mid height while for the other two it is not so clear. The explanation can be found in the increased angle of attack which shifts the canard vortex upwards. Indeed by looking carefully, the two new layouts exhibit a bigger top edge wheel vortex. Moving downstream at plane $z = -1.75$, what stands out is that in the reference configuration there is an inboard wake with more energy losses than for the other two even maintaining the same overall shape. As confirmation of the shifted top edge vortex, in this plane is evident the difference in strength of the top left vortex compared to the reference configuration. In the last plane, the flow shows some other discrepancies in the wake region. In the reference configuration more losses are concentrated in the lower region towards the chassis, whereas the other layouts have narrower pressure losses close to the chassis but an area in the middle wake is found to appear. This difference may be related to the different canard layout which affects the top wheel edge vortices.

Looking at the streamwise velocity (Fig. 4.9), it clearly shows that at plane $z = -1.75$ the baseline layout has a greater deficit close to the ground which moves inboard, thus confirming what previously has been described. At the following plane two things should be highlighted: the reference configuration has a bigger deficit on the outboard of the tyre and in the centre right behind the wheel profile, whereas the other two, especially the third one, show more reversed velocity in the inboard with an area developed more upwards. This is quite in accordance with the C_pT figures shown above.

Regarding the vertical velocity (Fig. 4.10), the baseline canard angle shows a greater region of downwash right behind the tyre, concentrated in the middle and inboard. The other two instead present downwash mixed with upwash in the lower wake region, thus explaining what shown in Fig. 4.8 at plane $z = -2.15$.

Also for this configuration, in Table 4.3 the wheel aerodynamic coefficients are shown. Despite what has been explained previously the third geometry presents a lower $C_{L_{wheel}}$.

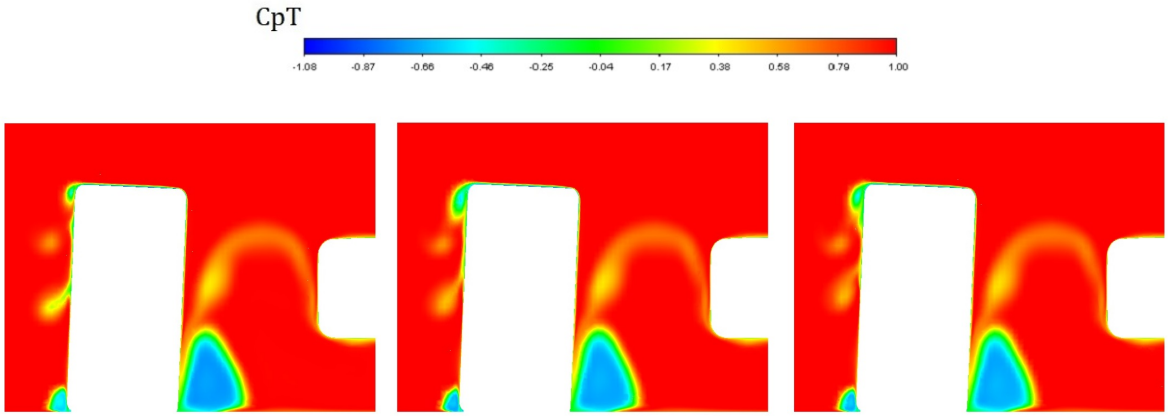

(a) *Plane* $z = -1.35$

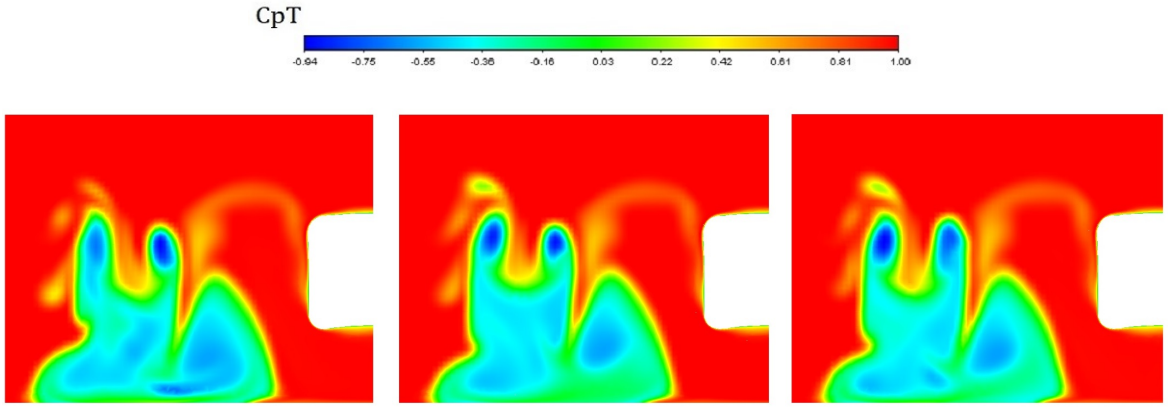

(b) *Plane* $z = -1.75$

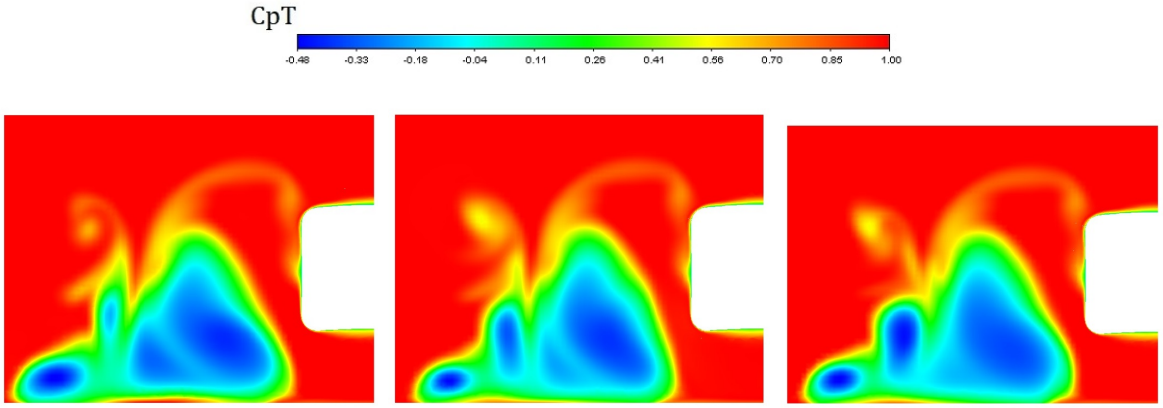

(c) *Plane* $z = -2.15$

Figure 4.8: Total pressure coefficient downstream of the wheel for canard with different angles of attack. It is possible to observe how the wake evolves towards the three planes for the three different configurations. From the left: baseline layout, 16° canard and 18° canard.

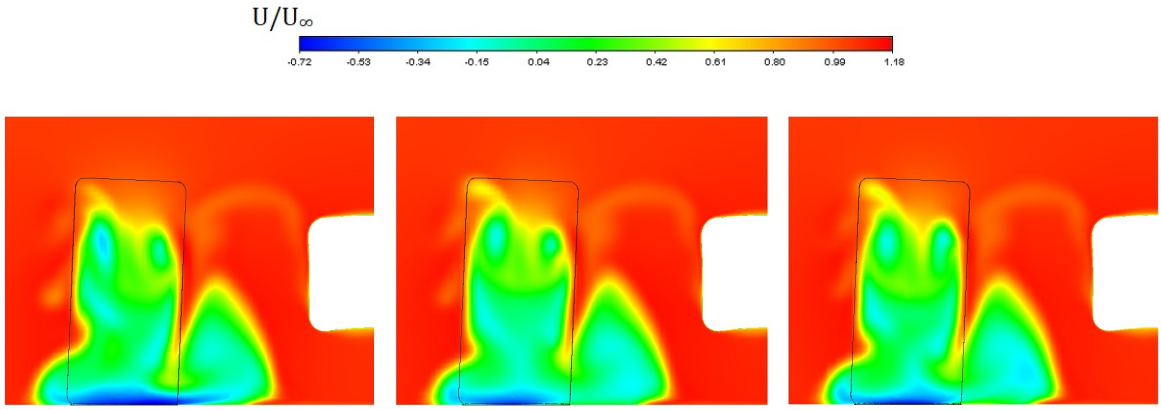

(a) *Plane* $z = -1.75$

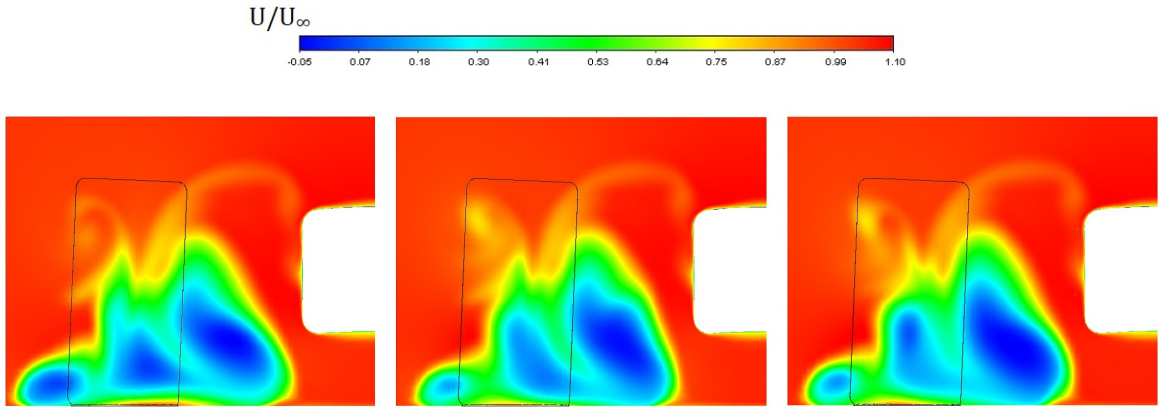

(b) *Plane* $z = -2.15$

Figure 4.9: Streamwise velocity in the wheel wake for canard with different angles of attack. From the left: baseline layout, 16° canard and 18° canard.

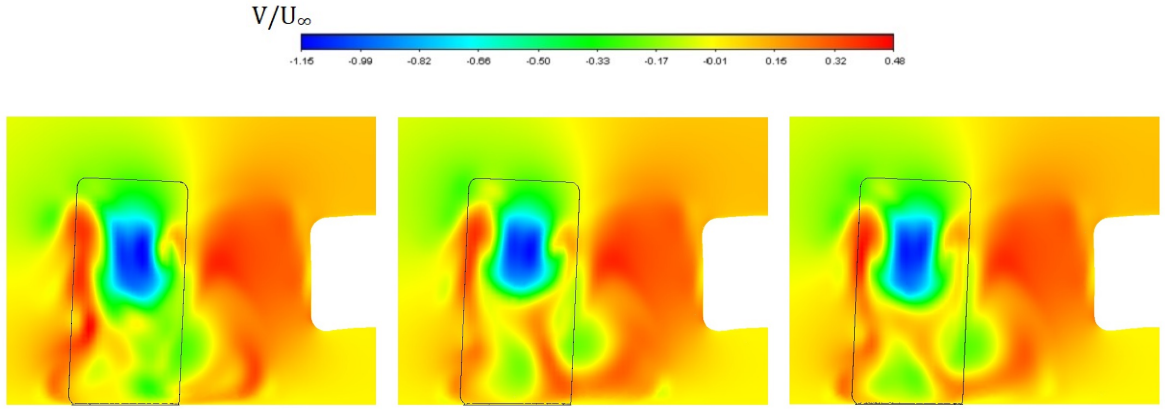

(a) *Plane* $z = -1.75$

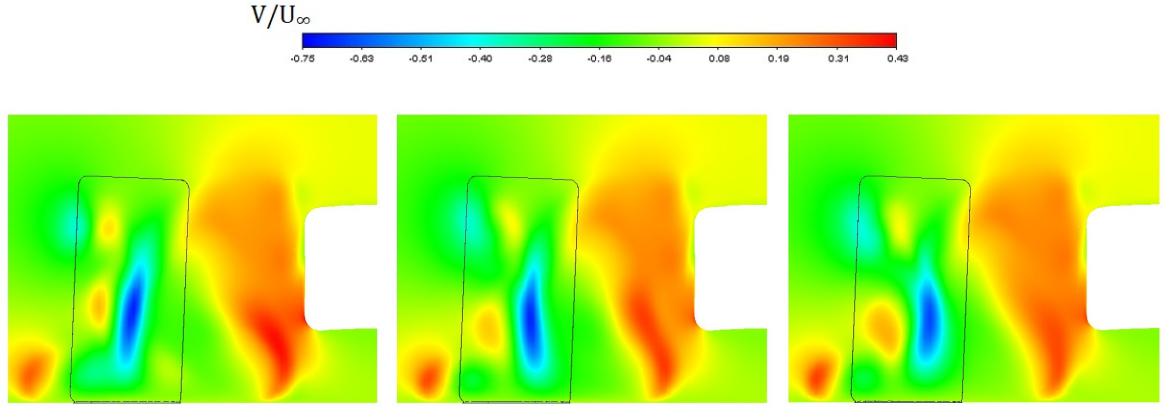

(b) *Plane* $z = -2.15$

Figure 4.10: Vertical velocity in the wheel wake for canard with different angles of attack. From the left: baseline layout, 16° canard and 18° canard.

Table 4.3: Wheel aerodynamic coefficients for the second configuration set.

	$C_{L_{wheel}}$	$C_{D_{wheel}}$
Reference layout	0.3631	0.3760
16° canard	+0.58%	−1.04%
18° canard	−2.23%	−0.51%

It may be caused by the higher AoA that favours the flow to move around the tyre and not be accelerated by its presence. Instead regarding the $C_{D_{wheel}}$, the second geometry shows a better value according to what has been shown in the wake description.

4.2.3 Endplate side shape analysis

In this third section the focus will shift to the modifications brought to the side shape of the endplate. Two new geometries will be analysed and compared to the usual reference one. The first one is a simple rectangular shape as the baseline one, with the difference lying in the height of this component. Instead of being $375mm$, it will be just $325mm$ differing by $50mm$. The third one is more interesting since it is one of the shapes proposed in the new prototypes by the FIA. This winglet is called shark fin[2], since its shape reminds the fin of the so called fish. This kind of layout has already been seen in Formula 1 in the 2010 season and then again in the 2017. However it was completely banned from the 2018 season. This component was added in the back of the monoposto behind the engine intake. From the next season we could probably see a reappearance of this device but on the front wing as a possible endplate layout. The side view designed is shown in Fig. 4.11.

Wing

For this new set of configurations greater discrepancies are shown in Fig. 4.12 regarding the C_pT distribution in wing flow. Concerning the shorter endplate, the vortex system preserves the same features but the losses in terms of energy are slightly less. In particular the region evolving from the lower edge vortex, is more confined. Instead for the shark fin endplate new considerations have to be done.

Looking at plane $z = -0.75$ it is clear how the new layout influences the top edge vortex and the canard one. The first is bigger than for all the other set of cases. This is related with the cut-out shape adopted which promotes the rolling up of the air from the pressure surface towards the outboard side of the endplate. Thus, this eddy has a bigger vortex core absorbing more energy. As a consequence of this new feature the canard

[2] *Previously adopted in the rear of the car, it is said to make the rear of the monoposto (diffuser) and rear wing more effective by proving a barrier to stop air crossing from one side of the engine cover to another, acting as a flow straightener, by aligning the airflow towards the rear wing and reducing turbulent air off the back of the airbox unit, and therefore 'cleaning' the air that enters the rear wing area, making the wing much more effective. That is why shark fin provide stability at the rear when going through high speed corners.*

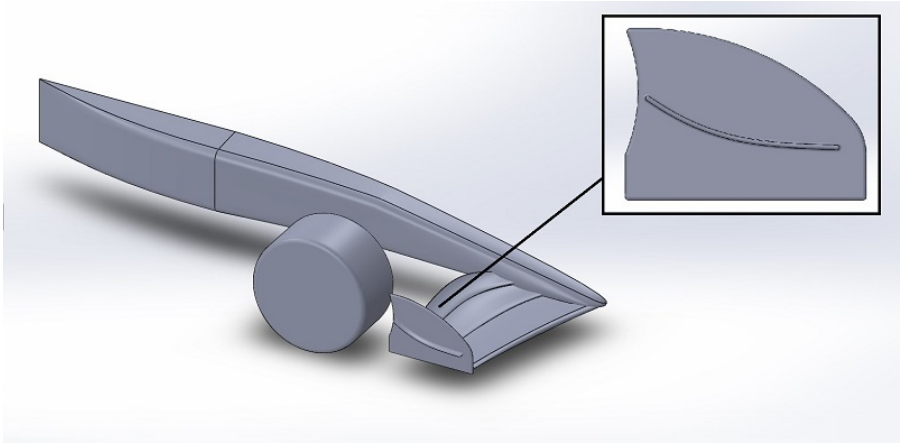

Figure 4.11: Shark fin endplate layout designed for this study.

vortex structure appears to be different from the previous analysis. Indeed the eddy resulting from the air rolling around the dive plate is less evident in all three planes. The presence of the shark fin plate favours the formation of the top edge vortex since the cut-out shape in the front of the endplate allows the air on the pressure side of the wing to roll up strongly than for the other cases. Anyway unlike the lower edge vortex, the top one does not face a breakdown, this is highlighted in Fig. 4.12 at plane $z = -0.95$. The structure of the vortex is restricted to a specific area with less losses and its core does not go through a bursting process.

Wheel

The analysis of the C_pT in the wake region (Fig. 4.13) allows for some interesting considerations. At plane $z = -1.35$, concerning the shorter endplate, the flow has more pressure losses near the tyre shoulder, while laterally, at mid height no pressure losses are so evident as for the baseline winglet. Instead getting closer to the top edge, confined losses are exhibited. This is related to the location of the top edge vortex of the shorter endplate. Since it is slightly downwards, the air separating on top of the wheel is less affected by its presence.

Regarding the cut-out configuration, always referring to the same plane, it is interesting to see that the top edge vortex is still visible. The strength of this vortex affects the fluid attached to the wheel side forming a shear layer which allows the formation of a bigger zone on the outboard. Regarding the inboard wheel, the cut-out shape configuration, shows a slightly smaller area of energy losses. This will affect the flow downstream the wheel, in the wake region.

At plane $z = -1.75$, the two new layouts shows a similar behaviour. The left vortex, of the two counter-rotating, is more defined and the pressure losses are well confined in a restricted area. The inboard of the wake, in the chassis proximity, shows less losses too. Indeed for the reference shape the inboard wake region is mixed with what is happening behind the wheel. This is worse in terms of energy losses because a more chaotic and uncontrolled flowfield is present. Whereas for the two new layouts, the inboard wake is quite split from the main wake zone. This flowfield will affect the wake

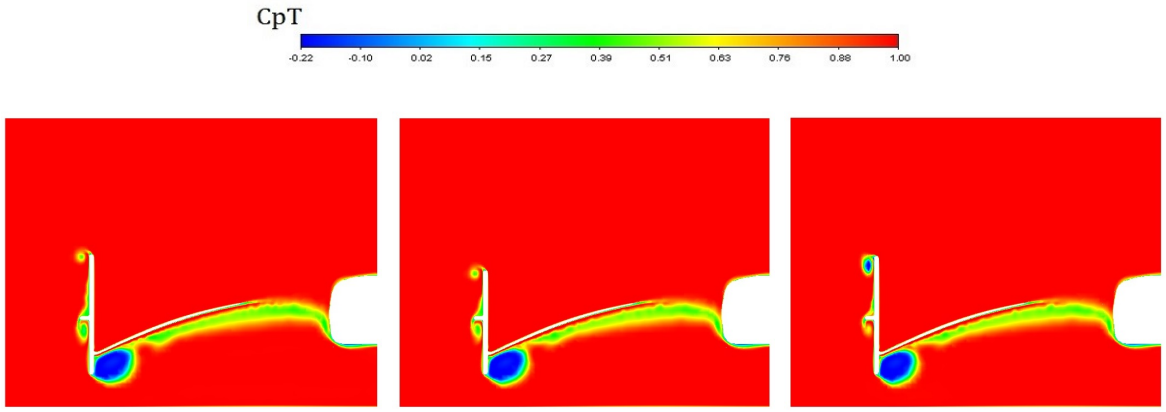

(a) *Plane* $z = -0.75$

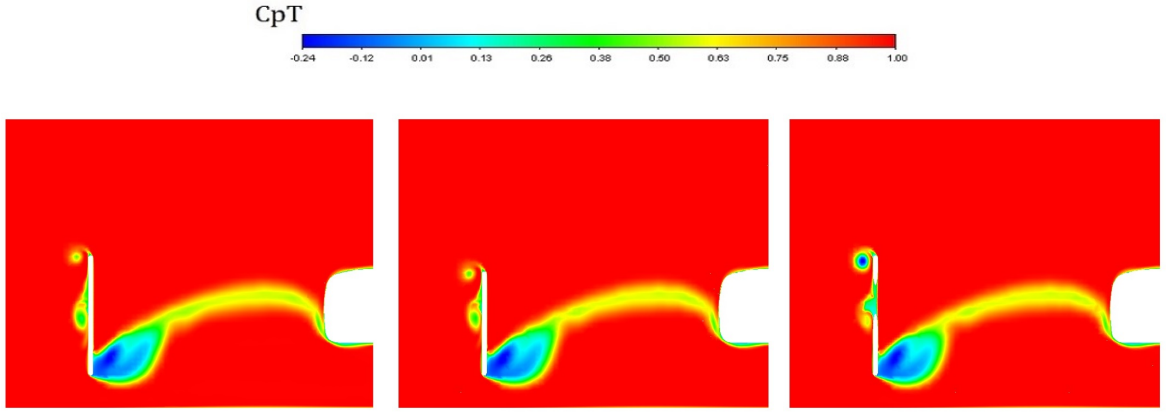

(b) *Plane* $z = -0.85$

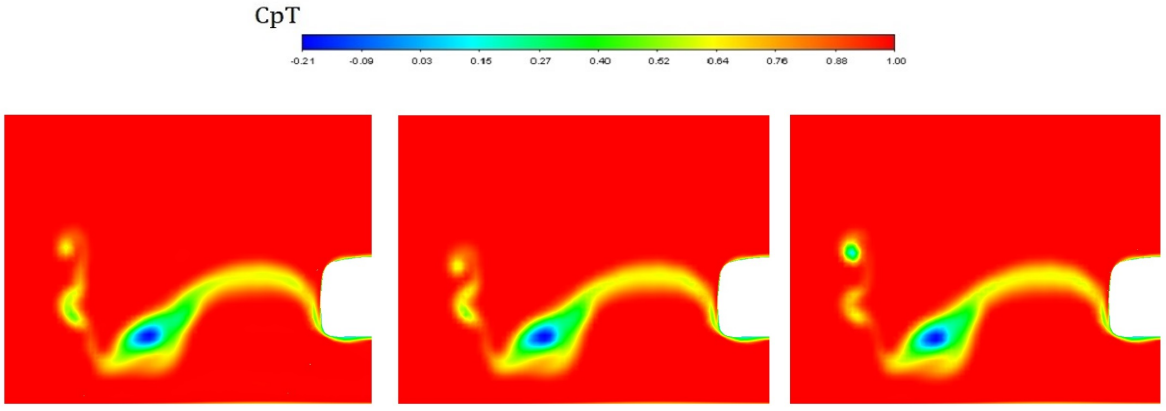

(c) *Plane* $z = -0.95$

Figure 4.12: Total pressure coefficient upstream of the wheel for different endplate side shape. It is possible to observe how the three vortices evolve towards the three planes for the three different configurations. From the left: baseline layout, shorter endplate and shark fin endplate.

Table 4.4: Wheel aerodynamic coefficients for the third configuration set.

	$C_{L_{wheel}}$	$C_{D_{wheel}}$
Reference layout	0.3631	0.3760
Shorter EP	−3.61%	−1.44%
Shark fin EP	+0.03%	+0.56%

further downstream. Moving at the last plane the difference just highlighted is more clear. The shorter endplate configuration has less losses with less dark blue areas and a narrower wake than the baseline one and is less shifted towards the chassis where the underbody intake is. The same can be said for the third one. The wake is more on the outboard, thus more exploitable energy is available to play with in the chassis proximity.

Regarding the streamwise and vertical velocities in the wake some considerations can be developed as well.

The streamwise velocity shows a greater deficit in the lower wake region for the baseline shape. Whilst for the cut-out endplate a greater deficit is evident in the outboard wake. The streamwise velocity confirms the behaviour seen in Fig. 4.13. Here the reference endplate shows a considerable deficit all over the wake area, in particular in the outboard zone.

Regarding the vertical speed in Fig. 4.15, a significant area of downwash is present in the baseline endplate. Whereas the other two show, as a confirmation of what seen in Fig. 4.13, two separated regions of downwash in the lower wake. This separation confirms what explained above. In the last plane, concerning the shark fin configuration, a further confirmation of a more available flow in the underbody's feeding process is shown. Underneath the chassis the flow has almost completely velocity in the streamwise direction with no upwash or downwash phenomena.

The wheel aerodynamic coefficients reported in Table 4.4 shows that the shorter endplate gives a better wheel load behaviour than the other two geometries even though, previously it was highlighted that the shark fin endplate gives a better performance regarding the underbody's feeding process. This is consistent with what has been represented before, the tyre wake area for the shorter endplate displayed less losses, i.e. a related lower $C_{D_{wheel}}$. Hence, one geometry may give more advantages on the wheel whereas the other on the underbody.

More information on the flow outboard of the wheel can be gathered by examining the vortices identified with the Q-criterion [6]. This method, as previously mentioned in Sec. 2.1, is useful not only as a vortex core identification method but also to visualise vortices. However one should be careful in the choice of the visualisation threshold, since it is still completely arbitrary. A lower value of this parameter can show a vortex merging while the same phenomenon for higher values can not be distinguish, thus it is important to keep in mind this when exploiting the Q-criterion. This method will show just what it is above the threshold chosen. Thus incrementing the limit only the stronger vortices will be displayed.

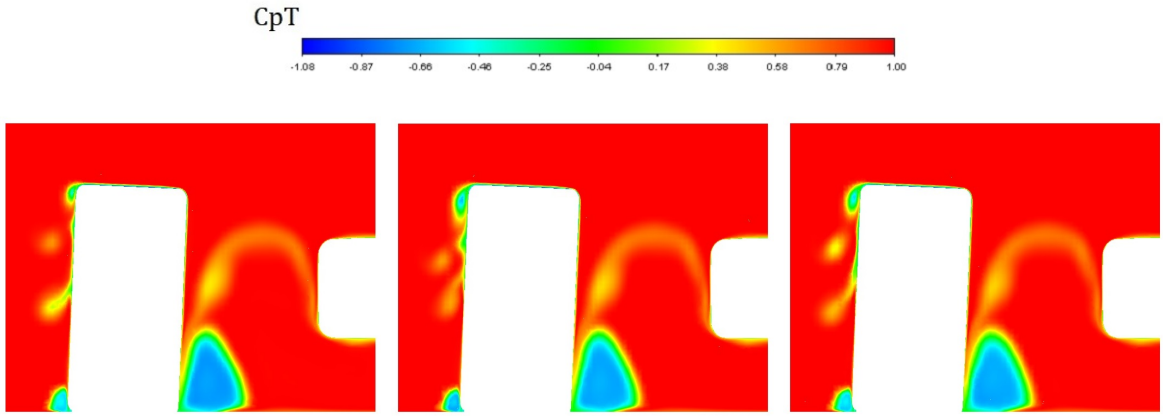

(a) *Plane* $z = -1.35$

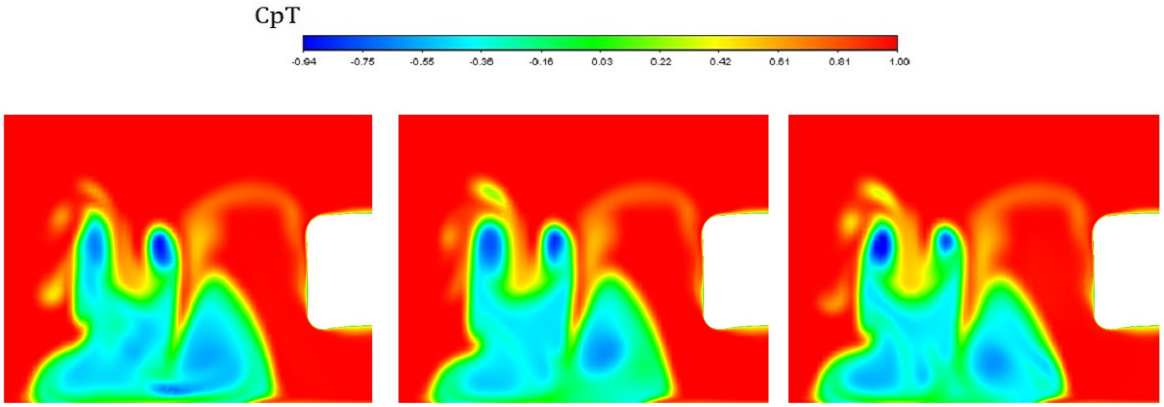

(b) *Plane* $z = -1.75$

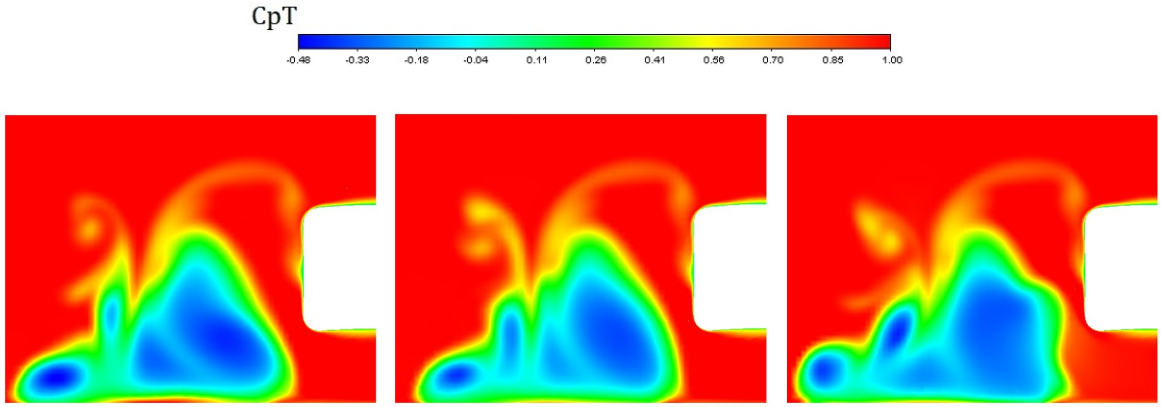

(c) *Plane* $z = -2.15$

Figure 4.13: Total pressure coefficient downstream of the wheel for different endplate side shape. It is possible to observe how the wake evolves towards the three planes for the three different configurations. From the left: baseline layout, shorter endplate and shark fin endplate.

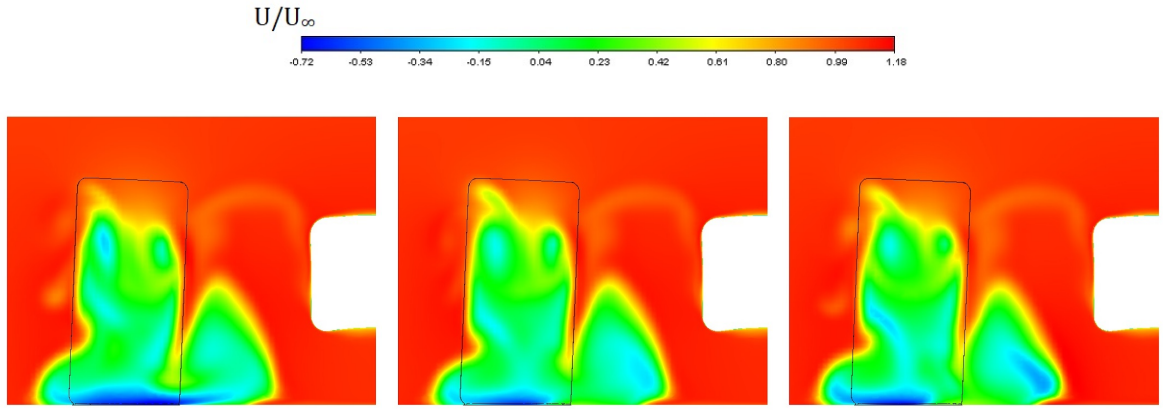

(a) *Plane* $z = -1.75$

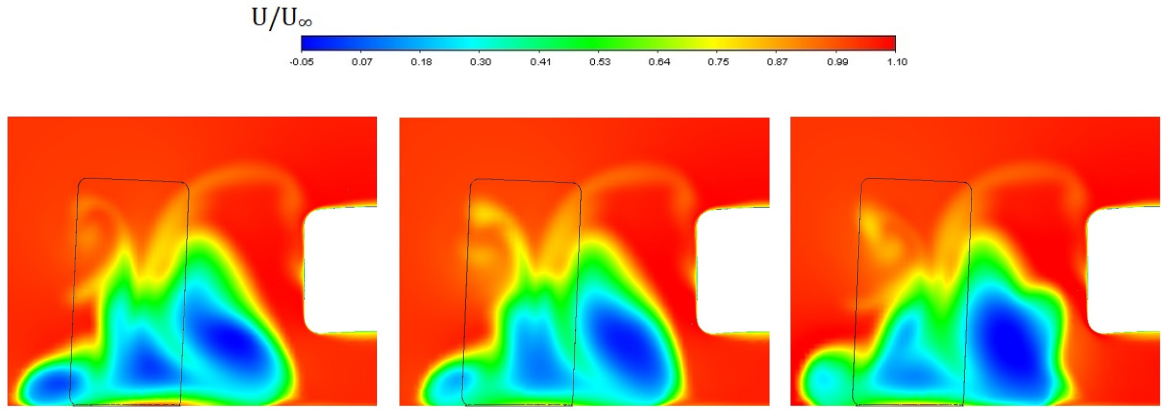

(b) *Plane* $z = -2.15$

Figure 4.14: Streamwise velocity in the wheel wake for different endplate side shape. From the left: baseline layout, shorter endplate and shark fin endplate.

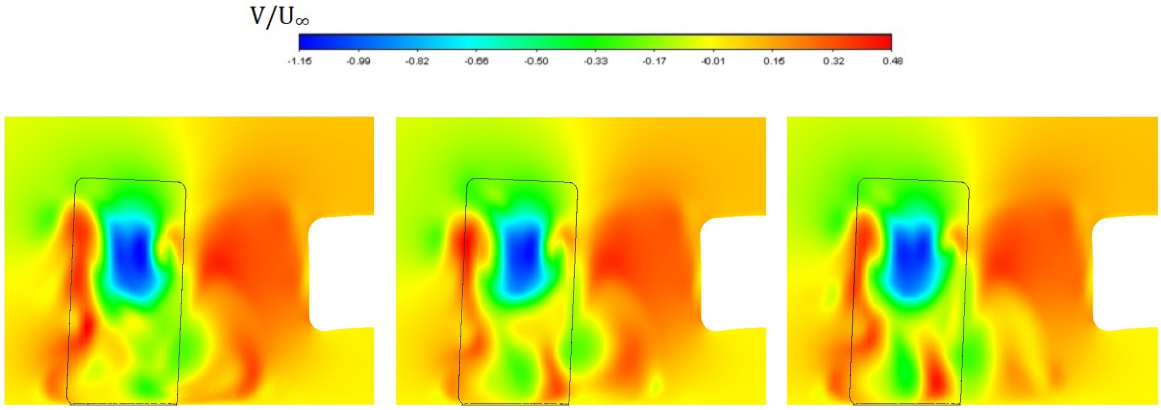

(a) *Plane* $z = -1.75$

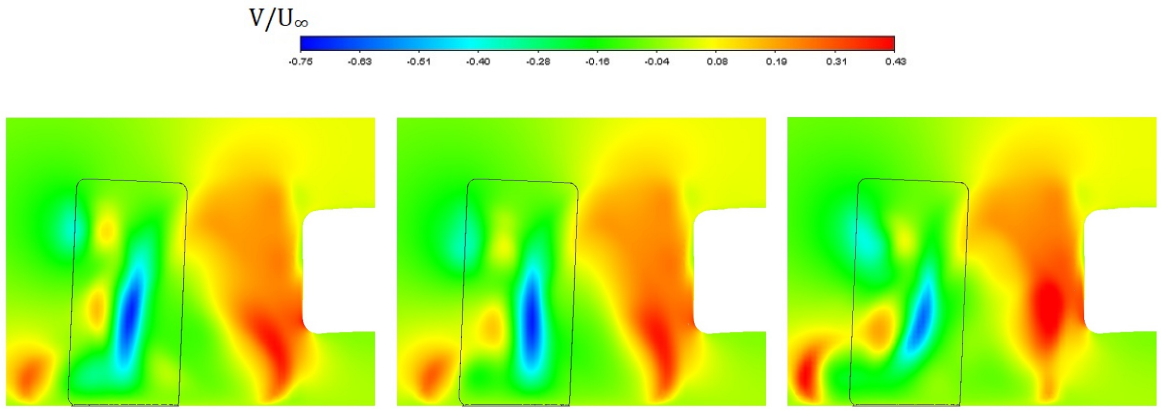

(b) *Plane* $z = -2.15$

Figure 4.15: Vertical velocity in the wheel wake for different endplate side shape. From the left: baseline layout, shorter endplate and shark fin endplate.

For a better visualisation of the vortex system shedding from the endplate, a side view of the swirling structures for all three configurations is presented in Fig. 4.16. The image shows the same features (i.e. top edge vortex, canard vortex and not so visible from this view, lower edge vortex), clearly, their position or behaviour change a little bit by modifying the endplate shape. The main difference lies in the top edge vortex, in particular for the shorter endplate case. As highlighted previously, this vortex is located downwards due to the geometry shape. This difference in the position compared to the reference configuration allows for less interaction with the top edge wheel vortex forming on the tyre shoulder. For this reason as we can see from this image and from Fig. 4.13, the vortex detaching and forming on the tyre shoulder is slightly bigger. Regarding the cut-out endplate no big differences can be found about the evolution of this vortex, anyway something can be pointed out about its formation process. This vortex due to the cut-out shape, begins to form slightly before than for the other two geometries. This happens, as explained previously, due to the modded leading edge of the endplate, favouring the rolling up of the air from the pressure surface to the outboard of the endplate.

4.2.4 Footplate analysis

In this last analysis a footplate will be added to the endplate, in Fig. 4.17 the design of this new component is available. Two different dimensions will be analysed. The one represented in Fig. 4.17 is the wider one, $40mm$ against the $20mm$ of the other configuration from the outboard of the endplate. The thickness is kept constant, with a corresponding value of $10mm$. The plate is flat, with no curvature in order to simplify the flow around it. It is not still clear if this component will be permitted for the next season, anyway it is interesting to understand what is the difference in adding or not an element like this to the endplate, considering that all the cars in the actual championship are equipped with a footplate.

Wing

First of all for this last configuration, it is very interesting to briefly discuss the aerodynamic forces acting on the wing. Unlike the other set of cases which did not altered as much the forces on the wing, the addition of the footplate greatly improves the downforce generated by this component. Compared to the reference values of the baseline geometry ($C_L = 1.9034$ and $C_D = 0.1781$), the new component increments the C_L by $+3.4\%$ for the wider case and $+1.5\%$ for the other one. This increase in downforce does not increase the drag as well, which instead decreases for both cases by -3.54%. This explains why all the cars nowadays are equipped with a footplate. Adding this component enhances the downforce without worsening the drag of the front wing. Anyway, even though obtaining better results in terms of aerodynamic performances on the front wing, it is necessary to explain that for this kind of application, i.e. race cars, an efficiency enhancement of a particular component may affect the efficiency of an other element or the whole car. Though when dealing with these kind of problems, one must keep in mind the goal is trying to achieve.

For a more detailed explanation, to understand why this device plays such an impor-

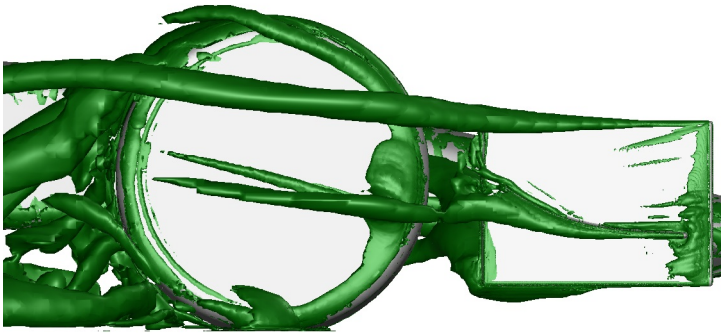

(a) *Reference EP*

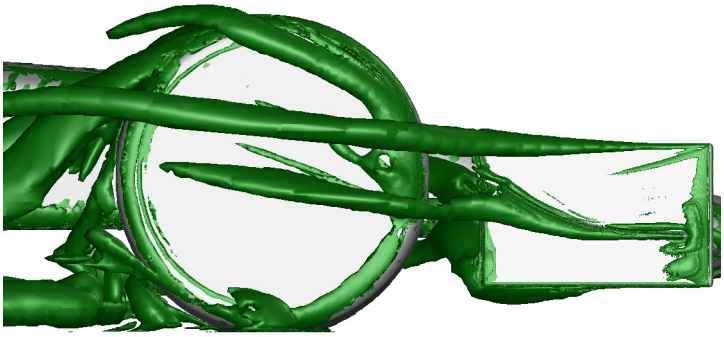

(b) *Shorter EP*

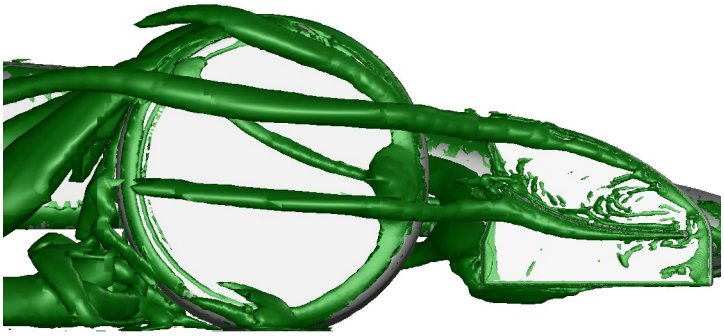

(c) *Shark fin EP*

Figure 4.16: Flowfield topology of the side view of isosurfaces of $Q = 100000$ for the side endplate analysis. The image shows the vortices shedding from the endplate for the three different geometries.

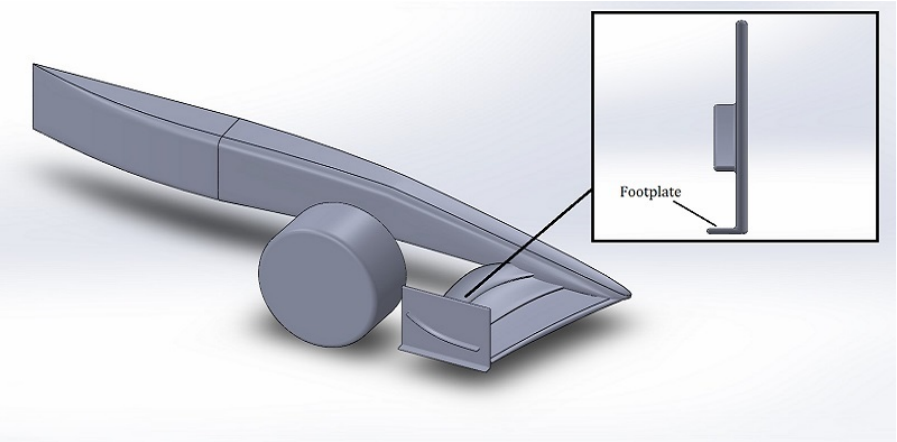

Figure 4.17: Footplate design added to the endplate structure. The current view represents the wider component, with a width of $40mm$ from the outboard of the endplate.

tant role, it is better to take a look to the C_pT in Fig. 4.18. This parameter will give a better insight to what happens by adding a footplate.

As already widely explained in this work the C_pT gives an overview to the pressure losses with respect to the freestream flow. With the addition of the footplate a detailed overview and deeper considerations should be done in order to clarify why there is such improvement in aerodynamic efficiency. The total pressure distribution is available in Fig. 4.18.

From the first plane $z = -0.75$, great differences stand out. The main discrepancy is located in the lower edge vortex as one would expect. This structure is directly affected by the presence of the footplate. Indeed by taking a look to the two new layouts, this latter vortex is going through a weakened breakdown process; which by increasing the width of the footplate gets smaller and smaller, reducing the pressure losses. This mechanism is the reason why the wing downforce undergoes such an increase since the vortex does not loose great amount of energy while travelling downstream.

The presence of the footplate increases the performance of the front wing. This component allows this mechanism by reducing the flow rolling from the outboard of the endplate to the suction surface sealing the flow like a skirt underneath the wing. Its edge favours the flow separation, thus the flow detaches loosing pressure, hence, since the air detached from this edge has already encountered total pressure reduction when getting in contact with the flow underneath the suction surface the gap is not so large as for an endplate without a footplate and the breakdown process weakens. Indeed for this latter layout, by observing the images towards the three planes, no pressure losses peaks are revealed, however a large area is shown. Anyway this zone does not show a negative total pressure hence the flow is not reversing but just stagnating or slowing down compared to the freestream. The same can be said for the $20mm$ plate even though the less wide component does not play the same effect. Therefore it can be said that a wider footplate increases the front wing efficiency and weakens the breakdown mechanism developing underneath.

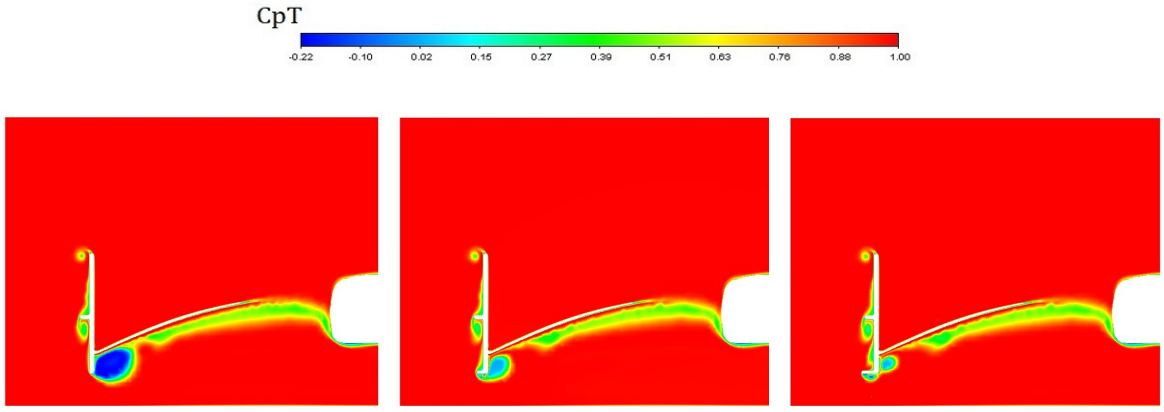

(a) *Plane* $z = -0.75$

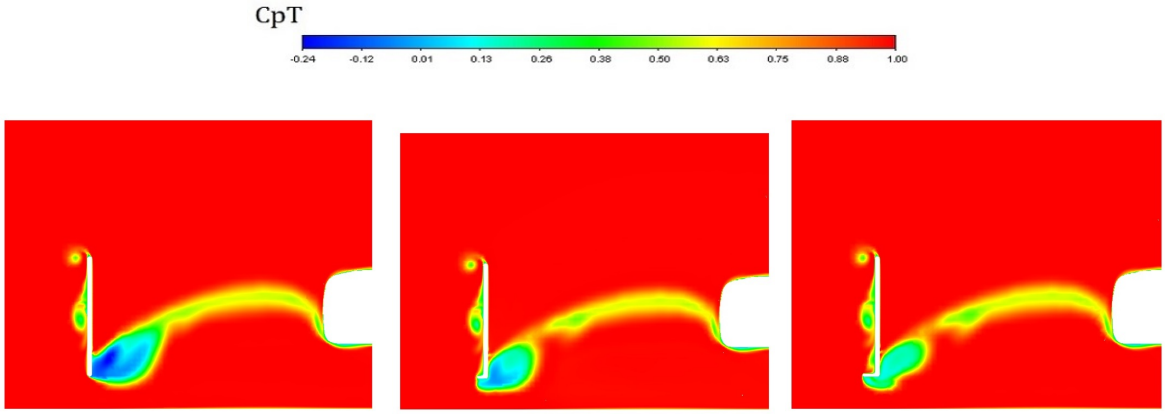

(b) *Plane* $z = -0.85$

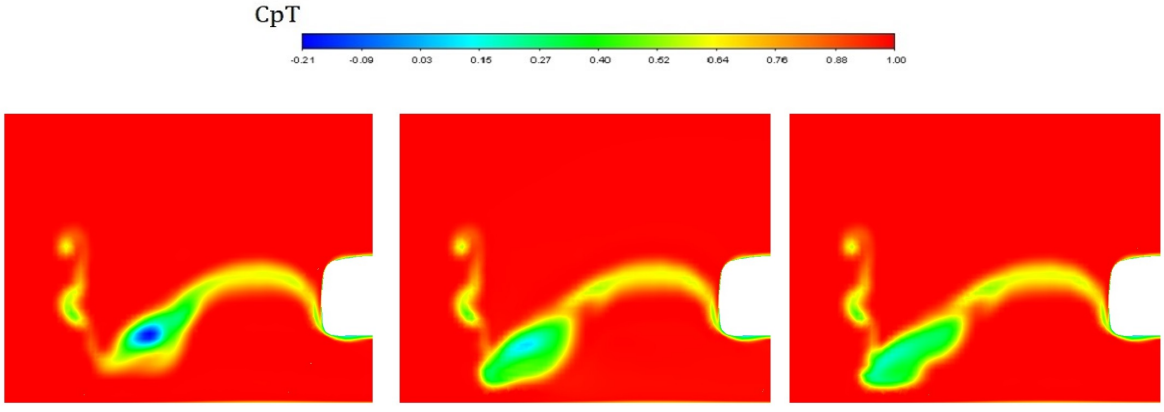

(c) *Plane* $z = -0.95$

Figure 4.18: Total pressure coefficient upstream of the wheel for the footplate configuration set. It is possible to observe how the presence of the footplate affects the flow around the wing. From the left: baseline layout, shorter footplate and wider footplate.

Wheel

The addition of the footplate clearly will affect the flow downstream the wheel in the wake region. The weakened lower edge vortex breakdown will modify the swirling flow.

First differences can be found around the wheel in the lower region at plane $z = -1.35$. From this view it is evident that the outboard lower vortex gets smaller and smaller as the footplate width increases, while at the same time loosing more energy. Indeed the pressure losses exhibited are greater, i.e. darker blue area. On the inboard instead the swirling region has about the same dimension but the pressure losses for an endplate equipped with a footplate are smaller. On the upper region nothing can be said or added since no discrepancies are shown, therefore the direct consequence is that an addition of a footplate does not affect the flow structure on the top of the tyre.

Moving to plane $z = -1.75$ some new features can be seen. The wake sees a restriction of the pressure losses on the outboard area, respectively for the two cases with a footplate. The interesting thing to point out is that a wider component reduces the pressure losses as Fig. 4.19 shows. Regarding the inboard of this swirling region, one can say again, that for a width increase reduces the losses, constraining more the blue and green area. About the upper wake, the flow behaves more or less in the same way. The only thing to highlight is the difference of the two counter-rotating vortices for the two cases with the footplate in comparison with the reference configuration. The left vortex shows more pressure losses than the right one.

For the last plane $z = -2.15$, where the underbody intake is placed, the flow shows again a total different behaviour. In presence of a footplate the wake close to the chassis is taller with greater losses confined more upwards. A circular area is visible in the centre. While moving outboard, the losses reduces more and more by increasing the footplate width. Between the two footplate layouts, a bigger component produces less energy deficit both in chassis proximity, in the centre and outboard, where the C_pT is ≈ 0. Therefore there is a stagnation region with no reverse flow.

Regarding the streamwise velocity (Fig. 4.20), it follows quite well the total pressure distribution. Starting from plane $z = -1.75$, one can identify that the presence of the footplate generates less velocity deficit in the wake region; and, as already widely explained, by increasing the footplate width these losses diminish. By moving at plane $z = -2.15$, the same trend keeps going, no losses, or very low, in the outboard region for the footplate case but greater deficit in the inboard, which, gets smaller and smaller by increasing the plate width.

By investigating the vertical velocity component in Fig. 4.21, further discrepancies can be highlighted. Adding a footplate increases the downwash region right behind the wheel. This difference explains the distinct wake size in that region. This behaviour might be related to less upwash located in the outboard zone. Regarding the last plane, it is evident less downwash for the footplate cases, this is connected to what happens upstream. A delayed downwash as for the reference configuration, increases the size of the wake, thus generating more drag on the upstream components, such as front wing. Furthermore in chassis proximity, a greater region of upwash is displayed for the footplate layouts, however it is more shifted upwards with lower values in the low region, close to the underbody. For this reason increasing the footplate width less upwash or

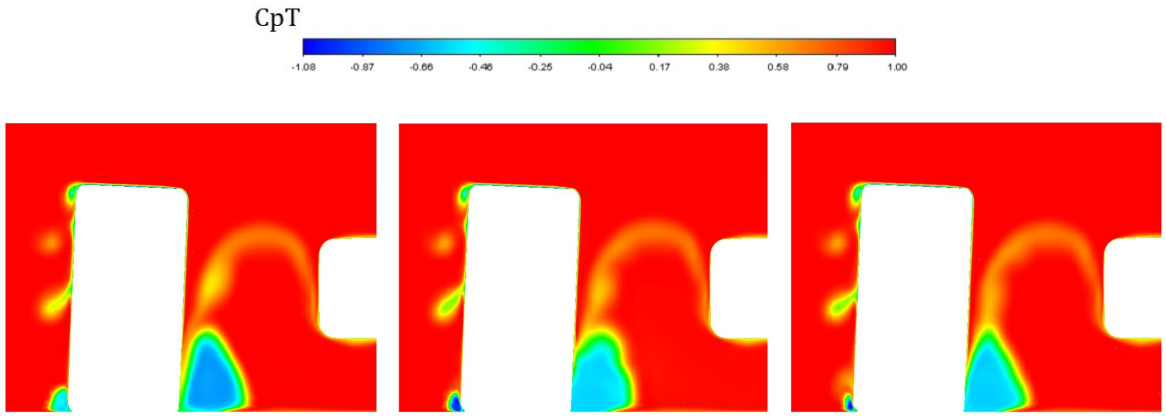

(a) *Plane* $z = -1.35$

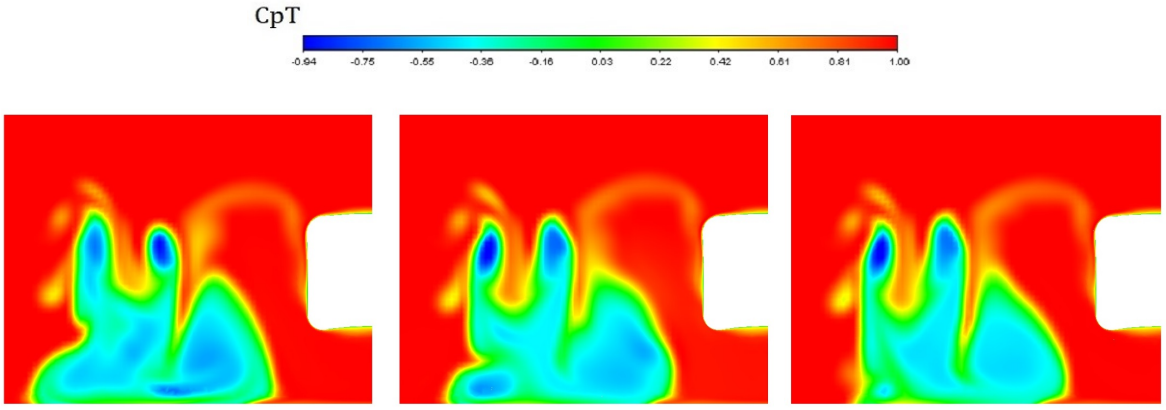

(b) *Plane* $z = -1.75$

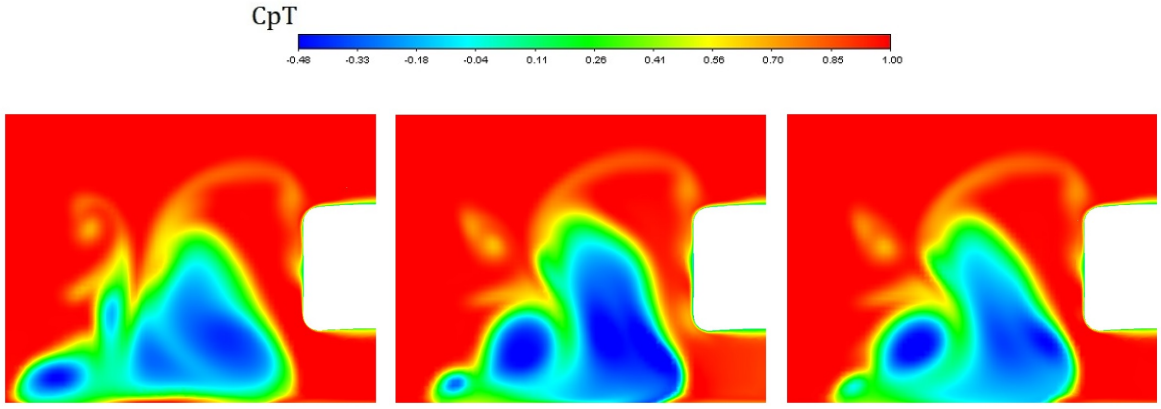

(c) *Plane* $z = -2.15$

Figure 4.19: Total pressure coefficient downstream of the wheel for the footplate configuration set. From the left: baseline layout, shorter footplate and wider footplate.

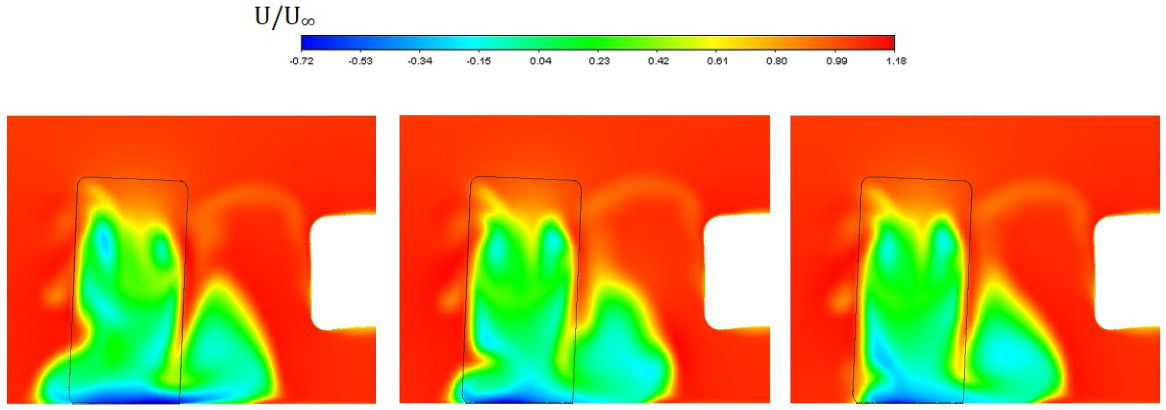

(a) *Plane* $z = -1.75$

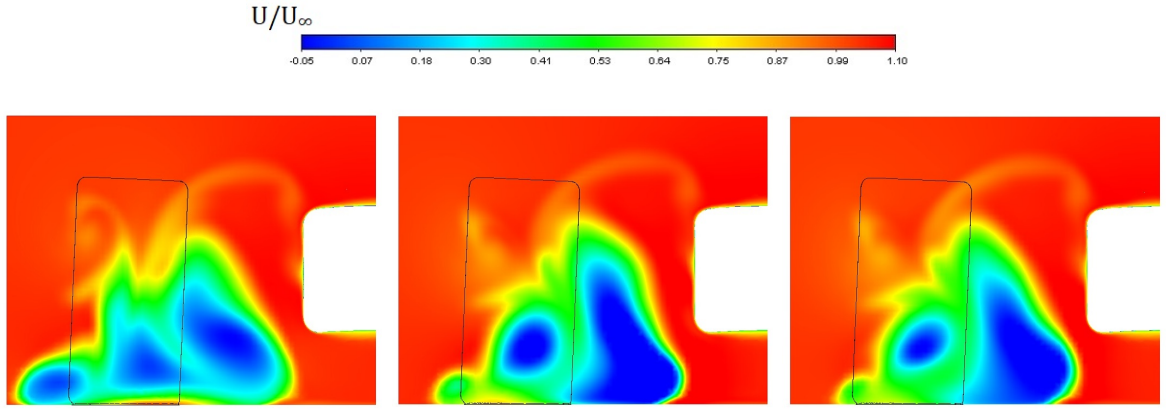

(b) *Plane* $z = -2.15$

Figure 4.20: Streamwise velocity in the wheel wake for the footplate configuration set. From the left: baseline layout, shorter footplate and wider footplate.

downwash phenomena are available in this region, hence more air is useful to feed the underbody.

Regarding the wheel aerodynamic coefficients something can be highlighted (Table 4.5). Despite enhancing the wing performance, the addition of the footplate increases the tyre lift, hence the wheel will have less grip on track. This may be related to the different flow coming towards the wheel due to the footplate presence, that may change too much the location of the stagnation point. This may induce the flow on top of the tyre to accelerate more, thus generating a bigger area of low pressure. Regarding the drag instead, the wider footplate confirms the good behaviour highlighted previously, diminishing its value. The shorter footplate, as Fig. 4.18 shows, due to the greater losses in the wheel wake area gives an higher drag coefficient.

For a more detailed discussion, it is interesting to introduce both non-dimensional vorticity contours and Q isosurfaces in order to visualise better the difference in the wake region and the vortices shedding from the front wing structure.

Looking at Fig. 4.22, it is possible to have a confirmation of what said previously. By adding and increasing the footplate width, one can see that the vorticity is more confined

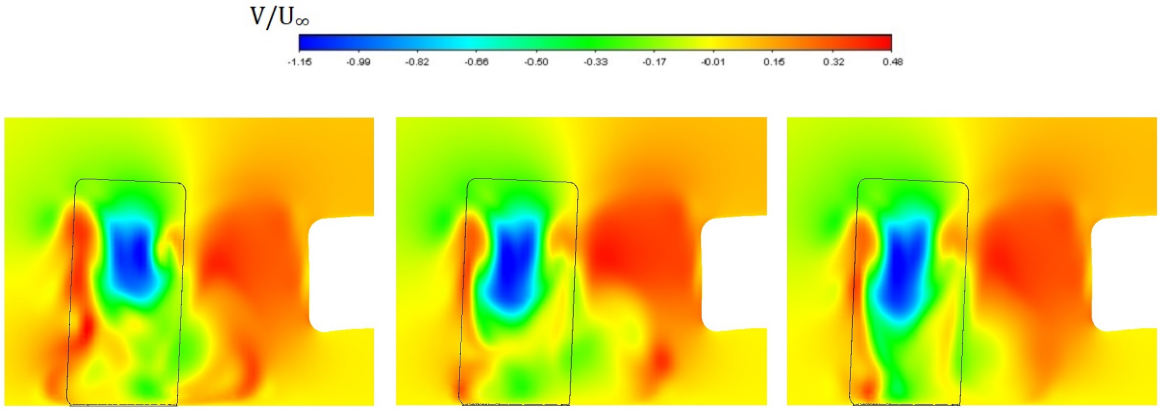

(a) *Plane* $z = -1.75$

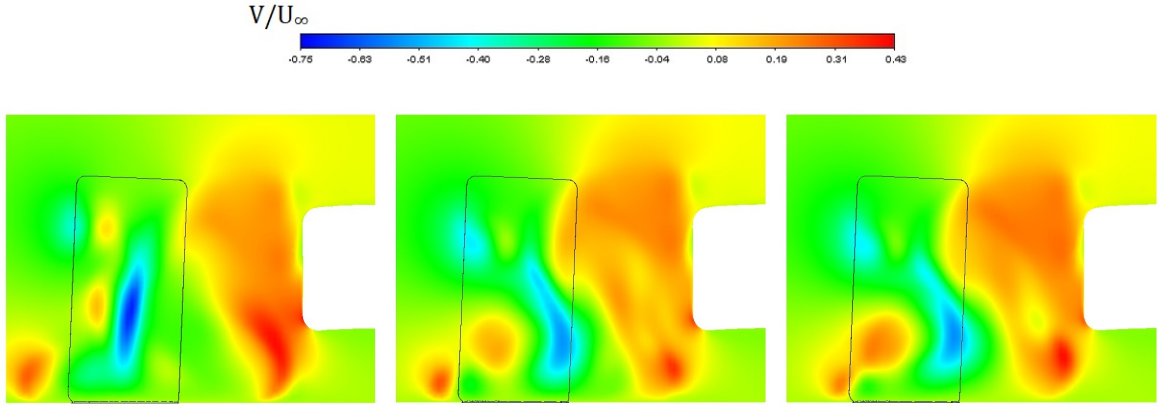

(b) *Plane* $z = -2.15$

Figure 4.21: Vertical velocity in the wheel wake for the footplate configuration set. From the left: baseline layout, shorter footplate and wider footplate.

Table 4.5: Wheel aerodynamic coefficients for the fourth configuration set.

	$C_{L_{wheel}}$	$C_{D_{wheel}}$
Reference layout	0.3631	0.3760
Shorter footplate	+6.44%	+2.00%
Wider footplate	+6.80%	−0.80%

right behind the tyre, with stronger vortices cores. Hence this can be an explanation to the front wing efficiency enhancement mechanism caused by the footplate addition. This latter device, reduces the losses and the breakdown process as already explained.

In Fig. 4.22, it is clear the presence of the footplate vortex and how this structure gets smaller and more confined by increasing the plate width. It is as much clear also as the wake, particularly in the lower outboard region, gets significantly smaller as already widely explained. This figure points out also the main characteristics of this set of geometries which has been widely highlighted previously; the presence of the footplate reduces the size of the lower edge vortex, hence reducing the breakdown strength and increasing wing performance. However, it is important to remind what it has been illustrated previously for the Q-criterion, a wrong threshold value can lead to wrong considerations. Therefore this qualitative representation is done just to have a better idea of the structures evolving in the system, to visualise in a different way the considerations done.

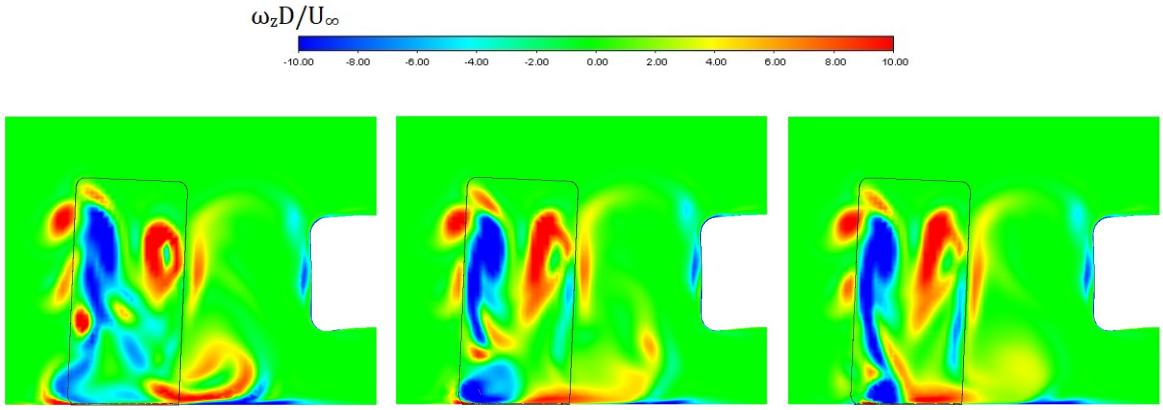

(a) *Plane* $z = -1.75$

Figure 4.22: Non-dimensional vorticity contours at plane $z = -1.75$ for the footplate configurations. From the left: baseline layout, shorter footplate and wider footplate.

(a) *Reference EP*

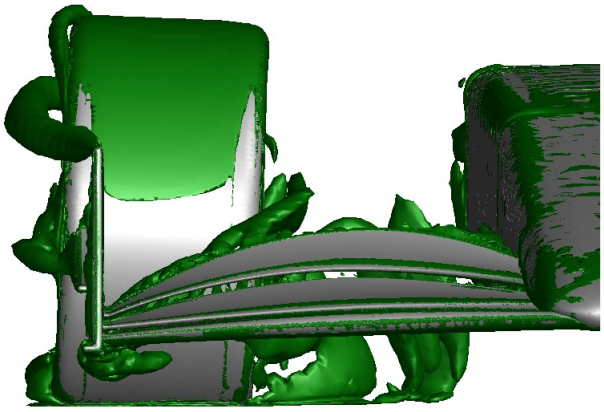

(b) *Shorter footplate*

(c) *Wider footplate*

Figure 4.23: Flowfield topology of the front view of isosurfaces of $Q = 100000$ for the footplate analysis. The image shows the vortices shedding from the endplate and front wing for the three different geometries. It is interesting to point out that the footplate presence, as its width increases, diminishes the wheel wake, making it narrower.

Chapter 5

Conclusions and Future Developments

5.1 Conclusions

In this final chapter a summary of all the relevant information gathered during this study will be exposed, keeping in mind all the problems and possible errors done during the whole process. Then some considerations about future works and further studies suggestions will be made.

A numerical study using a SRANS approach concerning the aerodynamics of an inverted three element wing, equipped with an endplate, and wheel was done. Following an analysis of the data collected, one can remark the following conclusions:

1. Since no aerodynamic optimisation has been performed during the design of the front wing, as expected, vortex breakdown does occur to the lower edge vortex, located underneath the suction surface. This is the case for almost all the configurations analysed, considering that for the footplate layout a different scenario develops increasing the width of the latter. The bursting process weakens by adding a footplate, thus, it would have been interesting to investigate which footplate width would have minimised the breakdown mechanism. This has serious implications on the wing performance, being one of the primary downforce limiting process as seen throughout this project.

2. The wheel wake can be divided into an upper and lower wake region. When comparing them both, the lower wheel wake extends further downstream, which is explained by the ground presence, the jetting effect occurring between the tyre and the ground and as seen for almost all the configurations by the presence of downwash within the wheel profile.

3. Regarding the canard location analysis, among the three configurations compared, no huge discrepancies have been found. Anyway, the lowest canard geometry exhibits a better behaviour in the wheel wake. The swirling flow shows less losses both inboard and outboard the tyre profile, thus leaving more energy to be exploited in proximity of the underbody intake. Furthermore, a "cleaner" wake

means less drag on the tyre. Other peculiarity regarding this set analysed can be found in the left vortex of the counter-rotating pair. By reducing the height of the canard, this swirling structure reduces the losses but expands its core, being more prone to breakdown.

4. The angle of attack of the canard has little to no influence on the wake structure. Few differences can be highlighted. The AoA variation changes a little bit the upper wake region, starting from the top surface of the tyre. A bigger top edge wheel vortex can be identified. This is the reason why further downstream the left vortex of the counter-rotating pair exhibits a more constrained core. In terms of losses, the 2° configuration shows an overall better behaviour, disrupting less the area of the intake.

5. The side shape analysis gave something more to discuss about. Concerning the wing flow, if the shorter endplate did not exhibit large differences, the shark fin shape instead, brought something new. The cut-out shape favours the roll up of air from the pressure surface to the endplate outboard. This mechanism reduces the canard eddy size while enhancing the top edge structure. The latter has a bigger core, clearly visible; nevertheless this vortex does not show signs of breakdown, being constrained in a well defined region. The shark fin frame helps in generating a wake region cleaner near the underbody. Both streamwise and vertical velocities confirm this trend. Hence the shark fin endplate could be a good component to increase the aerodynamic performance of the underbody. On the contrary the shorter endplate layout gives a better behaviour concerning the wheel loads.

6. The last analysis, in which a footplate of two different dimensions has been added, exhibits a new feature in the vortex system formation. The introduction of this component helps the front wing performance by isolating the flow underneath the wing acting like a skirt. The addition of a new swirling structure around its edge helps in reducing the pressure leap among the outboard of the endplate and the suction surface of the wing. Hence it is found out that by increasing the footplate size a smaller vortex is generated with lot less losses and a weakened breakdown mechanism. The restricted swirling area allows the wing to increase its efficiency since the bursting phenomenon does not occur in a strong way. Moreover, the addition of the footplate reduces the wheel wake size. If a shorter endplate shows a worst behaviour in the wheel wake concerning the tyre loads, a wider plate favours a smaller outboard wake region and less overall losses, thus promoting a cleaner flowfield, both behind the wheel and near the underbody intake.

7. The proof of a reduced breakdown process is given by looking at the forces arising on the front wing. The force analysis showed that by increasing the footplate width the wing efficiency increased, in particular the lift had a greater improvement than the drag, as a proof that the breakdown is a limitation in the lift enhancement mechanism.

5.2 Future Developments

The geometry designed for this thesis is a simplified version of what can be a real Formula 1 car. As explained in Sec. 3.1, the simplification adopted aimed to reduce the flow complexity. For a more realistic and accurate study, all the components have to be analysed with no exception, such as brake ducts, suspension arms, wheel hubs, tyre deflectors, etc. In particular, attention should be paid to the tyre deflectors, a new introduction with the new regulations [3], since their goal is to clean up the flow passing around the tyre managing the front wheel wake.

The mesh convergence just monitored the residuals and force coefficients behaviour, thus not focusing on other aspects such flow features evolution, e.g. vortex behaviour. For a better convergence and independence analysis one might verify if by changing convergence monitors or increasing mesh size, a better prediction of swirling structures can be achieved.

This latter suggestions could have been reached with higher computational resources and especially preferring an unsteady analysis rather than a steady one. For the reasons already explained the latter was chosen, however an unsteady approach such as URANS or DES could have shown different behaviours and more realistic results.

The project focused the attention just on the endplate geometry variation, reminding that many more endplate configurations could have been tested by performing an optimisation firstly in order to figure out which one would have been more significant. Regarding other aerodynamic components, it would have been interesting to see what changes and new feature a different flap angle of attack would have introduced. Since the aim of the thesis was to figure out the influence of the endplate on wheel wake, those changes have been neglected.

The entire geometry was made from the ground up with the help of a colleague of mine at UBI (Universidade da Beira Interior), who developed a parallel project involving the flap configuration. For this reason the model is unique in every detail; hence no direct comparable data, neither experimental nor numerical, are available for validation or verification. This step, hence, was attained through a pressure coefficient study. A more reasonable way of validating the computational results would have been by carrying a parallel experimental study alongside the numerical analysis.

The results obtained in this study and for the majority of projects done in the past years, both numerical and experimental, consider undisturbed and clean airflow. In order to have a more realistic insight of what happens on track, an idea could be to carry experiments in a tandem scenario, as it has been accomplished by Correia et al. [39], where a car follows another one. This would be more interesting and realistic and will have a better insight in understanding the new regulations introduced by FIA. Since they aim to increase overtakes and entertainment.

Bibliography

[1] J. Katz, "Race Car Aerodynamics: Designing for Speed", R. Bentley: Cambridge, MA, USA, 1996. ISBN: 978-0-8376-0142-7.

[2] J. Katz, "Aerodynamics of race cars", *Annual Review of Fluid Mechanics*, vol.38, no.1, pp.27-63, 2006. DOI: https://doi.org/10.1146/annurev.fluid.38.050304.092016

[3] FIA, "2022 Formula 1 Technical Regulations", 2020.

[4] ANSYS Academic Research Mechanical and CFD, Release 19.3, ANSYS, Inc.

[5] P.Chakraborty, S. Balachandar and R. Adrian, "On the relationships between local vortex identification schemes". *Journal of Fluid Mechanics*, vol.535, pp.189-214, 2005. DOI: https://doi.org/10.1017/S0022112005004726

[6] J. Jeong and F. Hussain, "On the identification of a vortex", *Journal of Fluid Mechanics*, vol.285, pp.69-94, 1995. DOI: https://doi.org/10.1017/S0022112095000462

[7] R. Cucitore, M. Quadrio and A. Baron, "On the effectiveness and limitations of local criteria for the identification of a vortex", *European Journal of Mechanics - B/Fluids*, vol.18, no.2, pp.261-282, 1999. DOI: https://doi.org/10.1016/S0997-7546(99)80026-0

[8] C. Cerretelli and C. Williamson, "The physical mechanism for vortex merging", *Journal of Fluid Mechanics*, vol.475, pp.41-77, 2003. DOI: https://doi.org/10.1017/S0022112002002847

[9] J. M. Delery, "Aspects of vortex breakdown", *Progress in Aerospace Sciences*, vol.30, no.1, pp.1-59, 1994. DOI: https://doi.org/10.1016/0376-0421(94)90002-7

[10] J. H. Faler and S. Leibovich, "Disrupted states of vortex flow and vortex breakdown", *Physics of Fluids*, vol.20, pp.1385-1400, 1977. DOI: https://doi.org/10.1063/1.862033

[11] T. Sarpkaya, "On stationary and travelling vortex breakdowns", *Journal of Fluid Mechanics*, vol.45, no.3, pp.545-559, 1971. DOI: https://doi.org/10.1017/S0022112071000181

[12] O. Lucca-Negro and T. O'Doherty, "Vortex breakdown: a review", *Progress in Energy and Combustion Science*, vol.27, no.4, pp.431-481, 2001. DOI: https://doi.org/10.1016/S0360-1285(00)00022-8

[13] J. Zerihan and X. Zhang, "Aerodynamics of a Single Element Wing in Ground Effect", *Journal of Aircraft*, vol.37, no.6, pp.1058-1064, 2000. DOI: https://doi.org/10.2514/2.2711

[14] X. Zhang and J. Zerihan, "Aerodynamics of a Double-Element Wing in Ground Effect", *AIAA Journal*, vol.41, no.4, pp.1007-1016, 2003. DOI: https://doi.org/10.2514/2.2057

[15] X. Zhang and J. Zerihan, "Edge Vortices of a Double Element Wing in Ground Effect", *Journal of Aircraft*, vol.41, no.5, pp.1127-1137, 2004. DOI: https://doi.org/10.2514/1.1380

[16] X. Zhang, W. Toet and J. Zerihan, "Ground Effect Aerodynamics of Race Cars", *Applied Mechanics Reviews*, vol.59, pp.33-49, 2006. DOI: https://doi.org/10.1115/1.2110263

[17] B. Agathangelou and M. Gascoyne, "Aerodynamic Design Considerations of a Formula 1 Racing Car", *SAE Technical Paper 980399*, 1998. DOI: https://doi.org/10.4271/980399

[18] J. E. Fackrell and J. K. Harvey, "The Flowfield and Pressure Distribution of an Isolated Road Wheel", *Advances in Road Vehicle Aerodynamics*, pp.155-165, 1973.

[19] J. E. Fackrell, "The Aerodynamics of an Isolated Wheel Rotating in Contact With the Ground", Ph.D. Thesis, University of London, UK, 1974.

[20] J. E. Fackrell and J. K. Harvey, "The Aerodynamics of an Isolated Road Wheel", *Proceedings of the Second AIAA Symposium of Aerodynamics of Sports and Competition Automobiles*, 1975. ISBN: 0879380284.

[21] J. McManus and X. Zhang, "A Computational Study of the Flow Around an Isolated Wheel in Contact With Ground", ASME, *J. Fluids Eng.*, vol.128, pp.520-530, 2006. DOI: https://doi.org/10.1115/1.2175158

[22] J. Axerio, G. Iaccarino, E. Issakhanian, K. Lo, C. Elkins and J. Eaton, "Computational and experimental investigation of the flow structure and vortex dynamics in the wake of a formula 1 tire", *SAE Technical Paper 2009-01-0775*, pp.1–9, 2009. DOI: https://doi.org/10.4271/2009-01-0775

[23] J. Axerio-Cilies, E. Issakhanian, J. Jimenez and G. Iaccarino, "An Aerodynamic Investigation of an Isolated Stationary Formula 1 Wheel Assembly", ASME, *J. Fluids Eng.*, vol.134, pp.1-16, 2012. DOI: https://doi.org/10.1115/1.4005768

[24] S. Pirozzoli, P. Orlandi and M. Bernardini. "The fluid dynamics of rolling wheels at low reynolds number". *Journal of Fluid Mechanics*, vol.706, pp.496–533, 2012. DOI: https://doi.org/10.1017/jfm.2012.273

[25] J. M. Pegrum, "Experimental study of the vortex system generated by a Formula 1 front wing", Ph.D. Thesis, Imperial College London, UK, 2007. DOI: https://doi.org/10.25560/12585

[26] W.P. Kellar, A.M. Savill and W.N. Dawes, "Formula 1 car wheel aerodynamics", *Sports Engineering*, vol.2, no.4, pp.203-212, 1999. DOI: https://doi.org/10.1046/j.1460-2687.1999.00030.x

[27] M. A. Van den Berg, "Aerodynamic Interaction of an Inverted Wing With a

Rotating Wheel", Ph.D. Thesis, University of Southampton, UK, 2007. URL: http://eprints.soton.ac.uk/id/eprint/49927

[28] M. A. Van den Berg and X. Zhang, "The Aerodynamic Interaction Between an Inverted Wing and a Rotating Wheel", ASME, *J. Fluids Eng.*, vol.131, 2009. DOI: https://doi.org/10.1115/1.3215942

[29] J. Heyder-Bruckner, "The aerodynamics of an inverted wing and a rotating wheel in ground effect", Ph.D. Thesis, University of Southampton, UK, 2011. URL: https://eprints.soton.ac.uk/207263/

[30] S. Pope, "Turbulent Flows". Cambridge: Cambridge University Press, 2000. DOI: 10.1017/CBO9780511840531

[31] F. Menter, "Zonal Two Equation k-w Turbulence Models For Aerodynamic Flows", *23rd Fluid Dynamics, Plasmadynamics, and Lasers Conference*, AIAA 1993-2906, 1993. DOI: https://doi.org/10.2514/6.1993-2906

[32] F. Menter, "Two-equation eddy-viscosity turbulence models for engineering applications", *AIAA Journal*, vol.32, no.8, pp.1598-1605, 1994. DOI: https://doi.org/10.2514/3.12149

[33] F. Menter, "A Comparison of Some Recent Eddy-Viscosity Turbulence Models", ASME, *J. Fluids Eng.*, vol.118, no.3, pp.514–519, 1996. DOI: https://doi.org/10.1115/1.2817788

[34] F. Menter, M. Kuntz and R. Langtry, "Ten years of industrial experience with the SST turbulence model", *Turbulence, heat and mass transfer*, vol.4, no.1, pp.625-632, 2003.

[35] D. C. Wilcox, "Reassessment of the scale-determining equation for advanced turbulence models", *AIAA Journal*, vol.26, no.11, pp.1299-1310, 1988. DOI: https://doi.org/10.2514/3.10041

[36] Mark Drela, "Xfoil: Subsonic airfoil developement system", 2000. URL: https://web.mit.edu/drela/Public/web/xfoil/

[37] XFLR5, Analysis tool for airfoils, wings and planes, Open-Source Software. URL: http://www.xflr5.tech/xflr5.htm

[38] J. D. Anderson, "Fundamentals of Aerodynamics", *McGraw Hill Education*, 6th ed., 2017.

[39] J. Correia, L.S. Roberts, M.V. Finnis and K. Knowles, "Aerodynamic characteristics of a monoposto racing car front wing operating in high turbulence conditions", *The International Vehicle Aerodynamics Conference*, pp.225-236, 2014. DOI: https://doi.org/10.1533/9780081002452.6.225